


Article

Bio-Precipitation of Carbonate and Phosphate Minerals Induced by the Bacterium *Citrobacter freundii* ZW123 in an Anaerobic Environment

Bin Sun ^{1,2,†}, Hui Zhao ^{1,2,†} , Yanhong Zhao ¹, Maurice E. Tucker ^{3,4}, Zuozhen Han ^{1,2,*} and Huaxiao Yan ^{1,*}

¹ College of Earth Science and Engineering, College of Chemical and Environmental Engineering, Shandong Provincial Key Laboratory of Depositional Mineralization and Sedimentary Minerals, Shandong University of Science and Technology, Qingdao 266590, China; sunbin2012@163.com (B.S.); zhsdust@126.com (H.Z.); zhaoyanhong65@126.com (Y.Z.)

² Laboratory for Marine Mineral Resources, Center for Isotope Geochemistry and Geochronology, Qingdao National Laboratory for Marine Science and Technology, Qingdao 266237, China

³ School of Earth Sciences, University of Bristol, Bristol BS8 1RJ, UK; glmet@bristol.ac.uk

⁴ Cabot Institute, University of Bristol, Cantock's Close, Bristol BS8 1UJ, UK

* Correspondence: hanzuozhen65@126.com (Z.H.); yhxzym@sdust.edu.cn (H.Y.);
Tel.: +86-532-86-057-055 (Z.H.); +86-532-86-057-625 (H.Y.)

† These authors contributed equally to this work.

Received: 19 November 2019; Accepted: 7 January 2020; Published: 13 January 2020



Abstract: In this study, a facultative anaerobic strain isolated from marine sediments and identified as *Citrobacter freundii*, was used to induce the precipitation of carbonate and phosphate minerals in the laboratory under anaerobic conditions. This is the first time that the ability of *C. freundii* ZW123 to precipitate carbonate and phosphate minerals has been demonstrated. During the experiments, carbonic anhydrase, alkaline phosphatase and ammonium released by the bacteria not only promoted an increase in pH, but also drove the supersaturation and precipitation of carbonate and phosphate minerals. The predominant bio-mediated minerals precipitated at various Mg/Ca molar ratios were calcite, vaterite, Mg-rich calcite, monohydrocalcite and struvite. A preferred orientation towards struvite was observed. Scanning transmission electron microscopy (STEM) and elemental mapping showed the distribution of magnesium and calcium elements within Mg-rich calcite. Many organic functional groups, including C=O, C–O–C and C–O, were detected within the biominerals, and these functional groups were also identified in the associated extracellular polymeric substances (EPS). Fifteen kinds of amino acid were detected in the biotic minerals, almost identical to those of the EPS, indicating a close relationship between EPS and biominerals. Most amino acids are negatively charged and able to adsorb cations, providing an oversaturated microenvironment to facilitate mineral nucleation. The X-ray photoelectron spectroscopy (XPS) spectrum of struvite shows the presence of organic functional groups on the mineral surface, suggesting a role of the microorganism in struvite precipitation. The ZW123 bacteria provided carbon and nitrogen for the formation of the biotic minerals through their metabolism, which further emphasizes the close relationship between biominerals and the microorganisms. Thermal studies showed the enhanced thermal stability of biotic minerals, perhaps due to the participation of the bacteria ZW123. The presence of amino acids such as Asp and Glu may explain the high magnesium content of some calcites. Molecular dynamics simulations demonstrated that the morphological change and preferred orientation were likely caused by selective adsorption of EPS onto the various struvite crystal surfaces. Thus, this study shows the significant role played by *C. freundii* ZW123 in the bioprecipitation of carbonate and phosphate minerals and provides some insights into the processes involved.

Keywords: anaerobic environment; *Citrobacter freundii*; biomineralization mechanism; Mg/Ca ratio; struvite; vaterite

1. Introduction

Microorganisms, especially bacteria, as an important part of the Earth's biosphere, can facilitate many geochemical processes. Extensive research has been undertaken on the biomineralization processes of carbonate and phosphate minerals in the past decades, and the significant roles that microorganisms play in these processes have been widely reported [1–11]. Many species of microorganisms have been used to induce the precipitation of carbonate and phosphate minerals, including cyanobacteria, halophiles, methanogens and sulfate-reducing bacteria [8,11–17]. Among these, halophiles play an important role in the precipitation of microbially-induced minerals in various natural environments with high salinity. For example, Deng et al. [4] used halophilic bacteria as experimental strains to successfully induce the precipitation of dolomite, and their results showed that EPS could provide the nucleation sites for the dolomite. Besides, dolomite was also obtained with the participation of the halophilic bacterium *Haloferax volcanii* DS52 in the study of Qiu et al. [3], and their results indicated that acidic amino acids (aspartic acid and glutamic acid) could promote the dehydration of the Mg^{2+} ions in the presence of free carboxyl groups. Cyanobacteria have also been widely used as experimental strains to induce mineral precipitation. Han et al. [18] reported a clear preferential orientation in the calcite induced by *Synechocystis* sp. PCC6803. Intracellular biomineralization of amorphous carbonate has been observed inside cyanobacterial cells [16,19]. Vasconcelos and McKenzie [20] induced the precipitation of dolomite using sulfate reducing bacteria in an anaerobic environment and proposed a new kind of microbial dolomite model. Another strain of sulfate-reducing bacteria, LVform6, was isolated and used to induce dolomite under anaerobic conditions at low temperature [21]. Phosphate minerals, e.g., struvite, can also be induced by other sulfate-reducing bacteria [15,22]. Although many species of microorganisms have been investigated to induce carbonate and phosphate mineral precipitation, the bacterium *Citrobacter freundii* has rarely been employed; hence, in this study *C. freundii* was used as the experimental strain.

The precise roles that bacteria play in the biomineralization process are still not clear; however, several consensuses have been widely accepted. First of all, many researchers have reported that bacterial metabolism causes a pH increase. Krause et al. investigated the impact of the *Alcanivorax* sp. strain on the precipitation of calcite, and they found that ammonia released by the bacteria played a significant role in the observed pH increase due to the fact that the hydration of ammonia can produce hydroxyl ions, resulting in an increase in alkalinity [23]. However, Zhuang et al. found that pH still increased when the concentration of ammonia had reached a plateau; they proposed that the further pH increase resulted from the combined effect of ammonia and carbonic anhydrase (CA) [7]. Secondly, many researchers have reported that the cell wall itself and EPS can act as nucleation sites [24–26]. Braissant et al. investigated the influence of exopolysaccharides and amino acids on the mineral phase and morphology and found that extracellular organic substances could act as nucleation sites [27]. Anaerobic metabolism for biomineralization has also been given special attention [21,22]. During the bacterial growth period, the pH changes of the medium, the concentrations of bicarbonate and carbonate ions, and the increasing sulfide content accompanied with decreasing sulfate due to anaerobic metabolism, have all been widely investigated [21]. Besides, free Mg^{2+} ions can be released from neutral ion pairs ($MgSO_4$) due to the reducing activity of sulfate [4]. These changes indicate the important roles played by bacteria in the biomineralization processes.

In addition to microorganisms, there are several physicochemical factors controlling biomineralization. The Mg/Ca molar ratio has been regarded as one of the most important factors. Carbonate and phosphate minerals induced by moderately halophilic bacteria at various Mg/Ca molar ratios have been investigated [28], and the results showed that only calcite was precipitated at Mg/Ca

ratio of 0, Mg-calcite and struvite were formed at Mg/Ca ratios of 1.63 to 7.4, and only struvite was precipitated at Mg/Ca ratio of 13.2. Mg/Ca ratios do not only affect the mineral phase but also the crystallinity. In the previous studies, with increasing Mg/Ca ratios, the crystallinity of monohydrocalcite induced by *Staphylococcus epidermis* Y2 decreased [29], whereas that induced by the halophile *Halomonas smyrnensis* WMS-3 increased [11]. Other factors that have been investigated include the presence of crystal seeds and the culture conditions. Guo et al. investigated biomineralization in energetic and calm environments [30], and demonstrated their effects on mineral morphology and size. Lin et al. used calcite and kaolinite as crystal seeds in the culture medium to induce carbonate minerals, and the results indicated that most minerals were precipitated on the cell surface rather than the crystal seeds [31].

In this paper, we report biomineralization experiments in an anaerobic environment using the sulfate-reducing bacterium *C. freundii* ZW123. This microbe occurs widely in sediments, in the soil, as well as within humans, and plays an important role in the nitrogen cycle, reducing nitrate to nitrite in the environment. The strain ZW123 was isolated, purified and identified through 16S rDNA and physiological and biochemical identifications. The biochemical parameters of the culture medium inoculated with the ZW123 strain were documented, including cell concentration, pH, CA activity and alkaline phosphatase (ALP) content. Minerals collected in the experimental groups were analyzed with powder X-ray diffraction (XRD), scanning electron microscopy (SEM), Fourier transform infrared spectroscopy (FTIR) and X-ray photoelectron spectroscopy (XPS). Thermogravimetric analysis (TG), derivative thermogravimetric analysis (DTG) and differential scanning calorimetry (DSC) were used to analyze the thermal characteristics of biotic and abiotic struvite. Molecular dynamics simulation was conducted using the Discover Module of Material Studio software 8.0 in order to have a better understanding of the preferred orientation and unique morphology of biotic struvite compared with chemical synthetic struvite. This study may provide some insights into the biomineralization mechanisms of carbonate and phosphate minerals.

2. Materials and Methods

2.1. Culture Medium

The composition of the enrichment medium includes NaCl 30 g/L, K_2HPO_4 0.5 g/L, NH_4Cl 1 g/L, $CaCl_2$ 0.1 g/L, $MgSO_4 \cdot 7H_2O$ 2 g/L, yeast extract 1 g/L, 60% sodium lactate 6 mL/L, Na_2SO_4 0.5 g/L, $Fe(NH_4)_2(SO_4)_2$ 0.5 g/L, ascorbic acid 0.5 g/L, and L-cysteine 0.5 g/L. Fe^{2+} in $Fe(NH_4)_2(SO_4)_2$ will react with S^{2-} to produce FeS precipitates, indicating the existence of sulfate-reducing bacteria. $Fe(NH_4)_2(SO_4)_2$, ascorbic acid and L-cysteine need to be filtered using 0.22 μm pore-sized filter membrane. The composition of the liquid purification medium was the same as the enrichment medium, and a solid purification medium was prepared by adding 1.5% agar to the enrichment medium. All experiments were conducted in an anaerobic incubator (QX-II anaerobic incubator, Yuejin Medica Instrument Co., Ltd., Shanghai, China).

2.2. Isolation and Identification of Bacterium Strain ZW123

Marine sediments were collected from the Tangdao Bay in Qingdao, China (120.1846° E, 35.9362° N). 20 g of marine sediments were added into 150 mL of the enrichment medium in the anaerobic incubator at 30 °C until the color turned black, indicating the existence of sulfate-reducing bacteria. Then 100 μL of the enrichment medium was diluted to 10^{-1} , 10^{-2} , 10^{-3} , 10^{-4} and 10^{-5} , respectively, and 20 μL of diluted bacterial solution was spread on the solid purification medium. Then the solid purification medium was also cultured in an anaerobic incubator at 30 °C until black colonies grew well. Then a single black colony was chosen and inoculated into the liquid purification medium. Three solid-liquid cycles were operated, and then a purified bacterial strain was obtained, namely ZW123. This purified bacterial strain ZW123 was then sent to Bioengineering Co. Ltd. (Shanghai, China) to obtain the 16S rDNA gene sequence. Gene sequence splicing was conducted using DNAMAN software (Version

6.0, Lynnon Biosoft Co., San Ramon, CA, USA), and then the spliced 16S rDNA sequences were uploaded to the NCBI website to obtain an accession number. Homology comparison of the 16S rDNA sequence between strain ZW123 and other bacteria in the NCBI database was also conducted. The phylogenetic tree of the strain ZW123 was constructed using MEGA (Version 6, The Pennsylvania State University, Philadelphia, PA, USA) with the Neighbor-Joining method [22,32]. The physiological and biochemical identifications, such as Gram stain, Vopes-Prokauer (VP) test, H₂S production, amylase test and bacterial motility test, and so on, were conducted according to previous studies [33].

2.3. Biochemical Parameters of Liquid Medium Inoculated by *C. freundii* ZW123

The bacterial strain *C. freundii* ZW123 was inoculated into the liquid medium and the cell concentration was tested until the value reached 0.8, then the preparation of liquid bacterial seed was finished. The liquid seeds were inoculated into the liquid medium at a volume ratio of 1.0%, and this was set as the experimental group; the liquid medium inoculated with the same volume of sterilized distilled water was set as the control group. The biochemical parameters of the liquid medium were then determined at regular time intervals. The cell concentration of the liquid medium in the experimental group was measured using a spectrophotometer (UNIC7200, Shanghai Sainity Hengfeng Scientific Instrument Co. Ltd., Shanghai, China); at the same time, pH was also measured with a pH meter (PHS-3E, Jiangfen Electrical Analysis Instrument Co. Ltd., Taizhou, China). An ammonia test was performed according to the published method [7]. CA activity and concentrations of carbonate and bicarbonate ions were measured with the methods described in a previous paper [7]. ALP activity was measured using the method described in [34].

2.4. Biotic Mineral Formation Induced by *C. freundii* ZW123

The medium used to induce mineral precipitation was prepared by adding MgCl₂ and CaCl₂ into the enrichment medium. The final concentration of Ca²⁺ was 0.01 M and Mg/Ca molar ratios were set as 0, 3, 6, 9 and 12. pH was also adjusted to 7.0. The medium was then sterilized using an autoclave sterilizer (LDZX-50KBS, Shenan, Shanghai, China). The liquid bacterial seed (see Section 2.3) was inoculated into the culture medium at a volume ratio of 1% and this was set as the experimental group; the control group was inoculated with the same volume of sterilized distilled water. Three identical samples were prepared for each Mg/Ca molar ratio. Both experimental and control groups were cultivated in the anaerobic incubator at 30 °C. Abiotic struvite was prepared according the method reported in a previous paper [35].

2.5. Characteristics of Minerals Induced by *C. freundii* ZW123

After 12 days of cultivation, precipitates were obtained from the experimental groups while no precipitates were obtained by filtration with a 0.22 µm pore-sized membrane from the control group. The precipitates from the experimental groups were collected and washed three times with distilled water, and then washed two times with anhydrous ethanol. The precipitates were then air-dried at room temperature, and analyzed using XRD (Ultima IV, Rigaku Corporation, Osaka, Japan) in an angle range of 10–60° and a scanning speed of 8° min⁻¹ [36–38]. Mineral phases of precipitates at various Mg/Ca ratios and the weight percent were analyzed using MDI Jade (Version 6.5, MDI Materials Data, Inc., Livermore, CA, USA) and Material Studio software (Version 8.0, Accelrys, San Diego, CA, USA). The morphologies and elemental composition of precipitates were analyzed using SEM (S4800, Hitachi, Tokyo, Japan) [39–45] and EDS (EDAX XM2-60S, Hitachi, Tokyo, Japan). The precipitates were also analyzed with Fourier transform infrared spectroscopy (FTIR, Nicolet 380, Thermol Electron Corporation, Waltham, MA, USA) [46–48] in the 4000–500 cm⁻¹ wavenumber range.

In order to further identify the relationship between minerals and organic matter, the organic substances within the minerals were also measured using FTIR. The minerals were washed using distilled water repeatedly in order to remove the organic substances on the mineral surfaces. The supernatant was then analyzed using FTIR. If the organic substances on the mineral surfaces were

removed completely, the FTIR spectrum would be identical with the distilled water. The minerals were then dissolved with 1% HCl solution and the hydrolysate was freeze-dried to powder; the powder was also analyzed using FTIR. The amino acid composition of the frozen powder was analyzed according to previous studies [29].

In order to further study the effect of ZW123 bacteria on the minerals and further determine the crystal structure of these precipitates, High-Resolution Transmission Electron Microscope (HRTEM) and selected area electron diffraction (SAED) analysis were conducted. The biotic mineral precipitates were fully ground in an agate mortar and then suspended with anhydrous ethanol. The suspension liquid was dripped on the copper net and analyzed using HRTEM (JEM-2100, Japan Electronics Company (JEOL), Tokyo, Japan) after natural drying. At the same time, SAED analysis of the corresponding nanometer area was done to determine the mineral crystal structure. The crystal lattice distance d (Å) were calculated with the electronic microscale software Digital Micrograph (Version 3.6.4, Catan Inc., Pleasanton, CA, USA). After the organic substances were completely washed off, struvite crystals collected in the experimental group at Mg/Ca ratio of 12 were also analyzed using XPS (Thermo ESCALAB 250XI, ThermoFisher, Waltham, MA, USA) with a step size of 0.05 eV. Charge correction was performed with O1s (530.90 eV) as standard binding energy [49].

2.6. Amino Acid Composition of EPS

EPS of bacteria ZW123 were extracted and the amino acid composition analyzed according to the method in the published paper [29]. In addition, the functional groups of extracted EPS powder were also analyzed using FTIR.

2.7. Thermal Characterization of Biotic and Abiotic Minerals

Thermogravimetric analysis (TG), derivative thermogravimetric analysis (DTG) and differential scanning calorimetry (DSC) were used to analyze the thermal characteristics of struvite. Biotic and abiotic struvite were dried at room temperature and ground into powder and then filtered with a 400-mesh sieve. The powder was then analyzed by a thermal analyzer (TGA/dsc1/1600lf, Mettler Toledo Co., Zurich, Switzerland) within the temperature range of 30–800 °C and at a heating rate of 10 °C min⁻¹. During this heating process, nitrogen was used as a protective gas to prevent oxidation. In addition, the thermal characterization of biotic monohydrocalcite at Mg/Ca molar ratios of 6 and 9 was also investigated in the temperature range of 30–900 °C and at a heating rate of 10 °C min⁻¹.

2.8. Stable Carbon and Nitrogen Isotope Analyses

In order to investigate the carbon source of the biotic carbonate minerals and then further understand the relationship between carbonate biomineralization and the microorganisms, stable carbon isotope values of biotic and abiotic carbonate minerals were determined through Isotope Analyzer (Picarro G2121-i, Picarro Inc., Santa Clara, CA, USA), according to the method in previous studies [50–55].

The nitrogen source of biotic struvite was also investigated. The stable nitrogen isotope of biotic struvite was analyzed using Stable Isotope Ratio Mass Spectrometry (MAT253, Thermo Fisher, Waltham, MA, USA) [56]. Stable nitrogen isotope values of inorganic nitrogen source (NH₄Cl) and organic nitrogen source (yeast extract) were also determined.

2.9. Molecular Dynamics Simulation of Glu Adsorption onto Struvite Surfaces

The adsorption capacity of glutamic acid (Glu) onto crystal faces of struvite was simulated using Material Studio software 8.0 (Version 8.0, Accelrys, San Diego, CA, USA). The molecular dynamics models for struvite and Glu were constructed and then the molecular dynamics simulation of the adsorption behavior of Glu was conducted. Parameter settings of molecular dynamic simulation for adsorption of Glu onto various surfaces of struvite were set according to Table S1. Then the adsorption energy was calculated to further investigate the selective adsorption of Glu onto each crystal face.

The adsorption energy of Glu onto different crystal faces of struvite is calculated by the following Equation (1):

$$E_{\text{adsorption}} = E_{\text{total}} - (E_{\text{Glu}} + E_{\text{surface}}) \quad (1)$$

where E_{total} represents the total energy of the whole system; E_{surface} and E_{Glu} represent the single point energies of the struvite surface and Glu molecule, respectively. All the calculations were also conducted using the Discover module of Material Studio software 8.0.

3. Results

3.1. Identification of Bacteria ZW123

The 16S rDNA sequence of bacterium ZW123 (GenBank accession number: MN416217) was 1485 bp in length, and shared over 99% homology with 54 strains of *C. freundii* using the Basic Local Alignment Search Tool (BLAST) in Genbank. As seen from the phylogenetic tree shown in Figure S1, strain ZW123 was most closely related with the *C. freundii* family. The results of the physiological and biochemical identification shown in Table S2 also proved that the characteristics of strain ZW123 were identical with those of *C. freundii* species in the published paper of Brenner et al. [57]. Therefore, strain ZW123 was identified as *C. freundii*.

3.2. Physicochemical Parameters of the Liquid Medium Inoculated with *C. freundii* ZW123

The bacterium *C. freundii* ZW123 is long-rod shaped, with a length of 1–1.5 μm and a width of about 0.8 μm (Figure S2a). Gram staining results proved that the *C. freundii* ZW123 bacterium is Gram-negative (Figure S2b). Before adding Nessler's reagent, the liquid medium in the experimental groups were turbid due to the presence of *C. freundii* ZW123 bacteria whereas the liquid medium in the control group was transparent (Figure S2c). After adding Nessler's reagent, the liquid medium in the experimental groups became brown-red and the color of the medium in the control group showed the color of Nessler's reagent (Figure S2d). The results indicated that *C. freundii* ZW123 bacterium was able to produce ammonia (NH_3). The ammonia released by the bacteria could be dissolved in the solution, and then ammonium and hydroxyl would be produced (Equation (2)). The increasing concentration of hydroxyl ions resulted in a pH increase in the fluid:



In Figure 1a, the growth curve of *C. freundii* ZW123 bacteria can be divided into four stages: an adaptation phase, logarithmic growth, a stationary phase, and a decline phase. In the first, adaptation phase, in the time range of 0 to 15 h, the cell concentration was nearly unchanged because the bacteria were gradually adapting to the new environment; the pH value declined from 7.10 to 6.84. The time range of the logarithmic phase was 15 to 52 h, in which period the pH increased from 6.84 to 7.60. The third phase was stationary phase between 52 to 63 h, when the cell concentration changed little, although the pH still increased. The last phase was a period of decline, in a time range of 63–156 h, when the cell concentration sharply decreased due to the consumption of nutrients and the gradual accumulation of harmful substances; pH increased to 8.02 at 126 h and then remained stable. However, in the control group the pH values were almost unchanged, near 7.0. Thus, it can be concluded that the presence of *C. freundii* ZW123 bacteria resulted in the pH increase in the fluid.

CA activity (Figure 1b) increased in the time range of 0 to 60 h, reaching a maximum value at 60 h (28.89 U/L). CA activity then showed a slight decline from 60 h to 156 h. From Figure 1b, it can be concluded that there was still a large amount of CA in the fluid even during the decline stage of ZW123 bacteria (Figure 1a). CA can catalyze the hydration of carbon dioxide to release bicarbonate and carbonate ions [32,58]. The concentration of bicarbonate increased from 0.02 mol/L to 0.036 mol/L in the first 48 h, declined from 0.036 mol/L to 0.0163 mol/L in the time range of 48–96 h, then almost remained stable until 156 h. Coinciding with the decline of the bicarbonate, the presence of carbonate

was first detected at 72 h; the concentration of carbonate then increased from 0.007 mol/L to 0.019 mol/L in the time range of 72–96 h, and then remained nearly stable. It may be inferred that the delay in the occurrence of carbonate ions was due to the process of conversion of bicarbonate ions into carbonate ions. From Figure 1b, it can be concluded that the concentration of carbonate ions reached a maximum value during the decline stage of the ZW123 bacteria. As shown in Figure 1a, the purple line indicates the change of pH based on the concentration of bicarbonate and carbonate ions. From 0–70 h, whenever the concentration of bicarbonate ion increased or decreased (Figure 1b), pH values did not change (purple line, Figure 1a); pH values sharply increased (purple line, Figure 1a) when the concentration of carbonate increased (Figure 1b), and pH was nearly stable (purple line, Figure 1a) when the concentration of carbonate ions kept constant (Figure 1b). The result indicates that the concentration of carbonate ions which originated from CA activity played an important role in the pH increase in this study. The other kind of enzyme ALP was also investigated in this study. ALP activity released by *C. freundii* ZW123 was not detected until 12 h and it increased rapidly from 4.31 U/L to 10.78 U/L in the time range of 12–86 h and decreased slightly to 7.33 U/L at 120 h (Figure 1c).

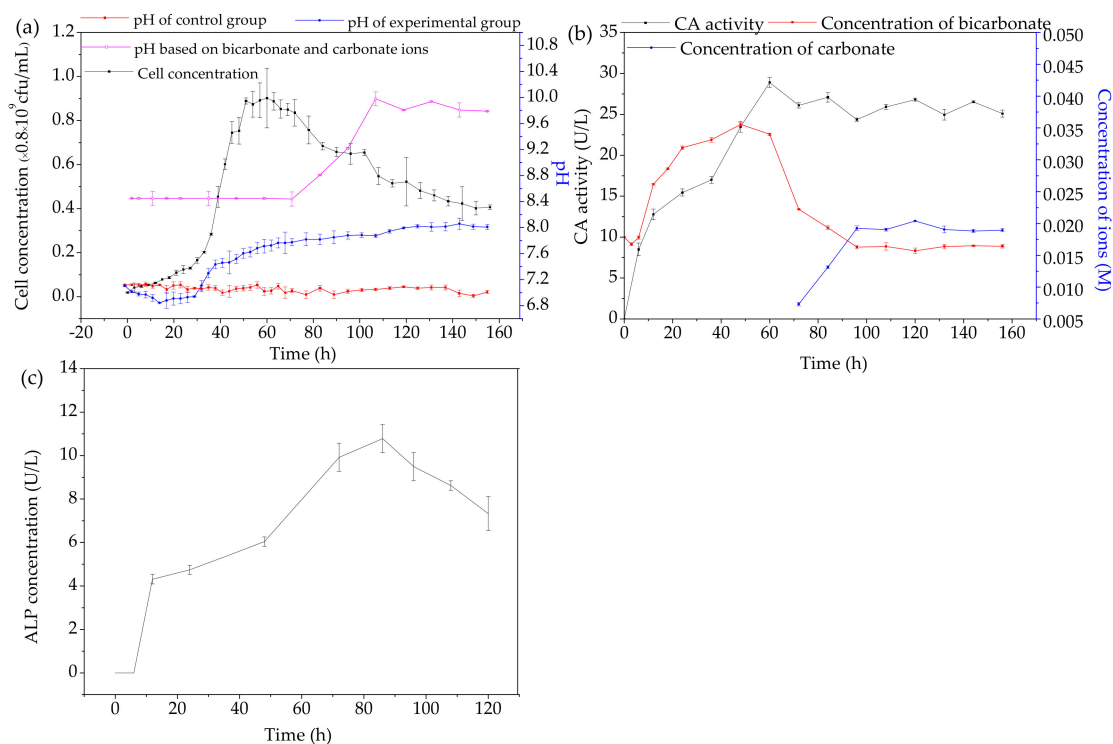


Figure 1. Concentration of *C. freundii* ZW123 bacteria and different pH curves (a) and CA activity and concentration of carbonate and bicarbonate ions (b) and ALP activity of ZW123 bacteria (c).

3.3. Characteristics of Minerals Induced by *C. freundii* ZW123

3.3.1. XRD Analyses and Rietveld Refinement

As shown in Figure 2, the mineral phases of the precipitates collected in the experimental group were analyzed by XRD. The mass ratios of minerals in the mixture were also calculated by Rietveld refinement, which is shown in Figure S3. It can be seen from Figure 2 that the harvested minerals are a mixture of calcite (97.2%) and vaterite (2.8%) (Figure S3a) at Mg/Ca ratio of 0; at the Mg/Ca ratio of 3 the precipitate is Mg-rich calcite. At Mg/Ca ratios of 6 and 9 only monohydrocalcite was obtained. No phosphate minerals were detected in the fluids with these Mg/Ca molar ratios. From Figure S3b–d, the simulated and the experimental line fits well, confirming that the determined phases are correct. It can be seen from Table 1 that the density of monohydrocalcite decreases with the Mg/Ca molar ratio increasing from 6 to 9, and the crystallinity of monohydrocalcite also decreases due to an

increase in the values of full width at half maximum (FWHM) of some crystal planes with increasing Mg/Ca molar ratios. These results suggest that higher concentrations of Mg^{2+} ion would destroy the crystal structure of monohydrocalcite even if the Mg^{2+} ions play an important role in the formation of monohydrocalcite.

At Mg/Ca ratio of 12, only the phosphate mineral struvite ($NH_4MgPO_4 \cdot 6H_2O$) was obtained; carbonate minerals were absent. Rietveld refinement also proved the mineral was struvite (Figure S3). For chemical struvite, the intensity of the crystal face (020) is stronger than that of the (011) plane; however, the opposite is the case for the struvite induced by *C. freundii* ZW123 (Figure 2), indicating the presence of an obvious preferred orientation. The lattice parameters (a,b,c) of struvite induced by *C. freundii* ZW123 are 6.809, 11.155 and 6.124, respectively; these are different from those of chemical struvite at 6.955, 11.218 and 6.142 [59]. This difference indicates that lattice defects and/or lattice distortion may have developed. The density of struvite induced by the ZW123 bacterium is 1.752 g/cm^3 , higher than that of chemical struvite (1.701 g/cm^3), suggesting that the biotic struvite has a denser crystal structure.

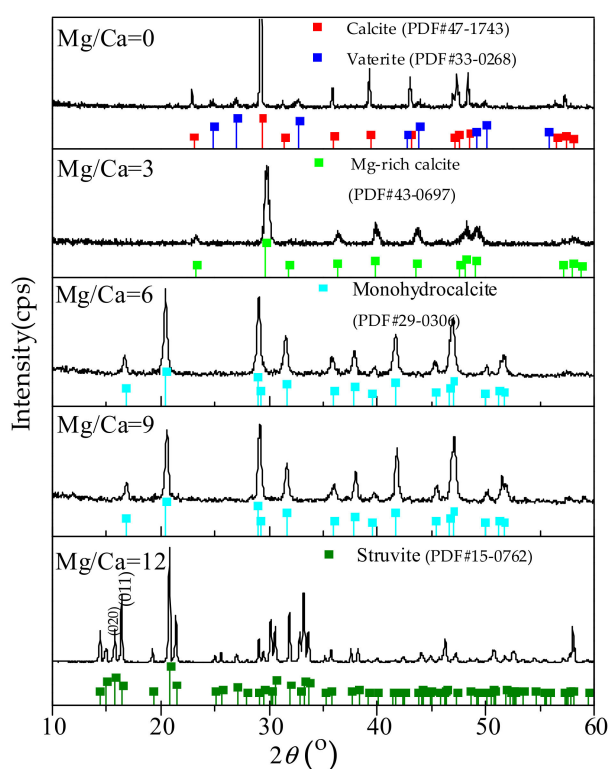


Figure 2. XRD analyses of minerals in the experimental groups after 14 days of cultivation.

Table 1. Parameters of monohydrocalcite at Mg/Ca molar ratios of 6 and 9.

Mg/Ca Ratio	Density (g cm^{-3})	FWHM (110)	FWHM (111)	FWHM (221)	FWHM (302)	FWHM (113)	FWHM (222)	FWHM (411)
6	2.4117	0.106	0.155	0.183	0.141	0.174	0.141	0.279
9	2.4076	0.131	0.163	0.196	0.184	0.337	0.175	0.314

3.3.2. Molecular Dynamics Simulation Results

As can be seen in Figure S4, the temperature and energy decreased rapidly and remained nearly stable with weak fluctuation, indicating equilibrium of temperature and energy and a stable system formed after the adsorption reaction of Glu on to the struvite crystal faces. The models of the (111) surface before and after adsorption were obtained (Figure 3c,d), and it is obvious that the Glu molecule

is much closer to the crystal surface after adsorption. It is noteworthy that the C=O functional group of Glu turned and approached the crystal surface (Squares in Figure 3c,d), indicating that the C=O group of Glu plays a key role in the adsorption process. Apparent deformation of Glu can also be observed (Figure 3c,d). Adsorption energies of Glu on different crystal surfaces are themselves different (Table 2), which indicates that the affinity of Glu for different crystal faces is quite variable. Glu could inhibit growth of crystal faces, and its inhibition effects on different crystal faces were also diverse.

The obvious preferred orientation of struvite induced by the ZW123 bacterium is also shown in the XRD pattern (Figure 2). For standard struvite, the intensity of the (020) faces is stronger than the (011) faces according to the XRD standard spectrum (Figure 2); however, the intensity of the (011) faces is stronger than that of (020) faces for bacterially-induced struvite. We assume that Glu may preferentially bind to (011) faces rather than (020) faces, and finally retard crystal growth of the (011) faces. According to the simulation results (Table 2), the adsorption capacity of Glu on to (011) was stronger than that of (020) faces; this means that there was a much stronger inhibition effect on the crystal growth of the (011) faces than (020) faces. As a result, more (011) faces are inhibited and a stronger intensity of (011) is present, which confirms our hypothesis and also indicates the selective interaction of Glu with these faces.

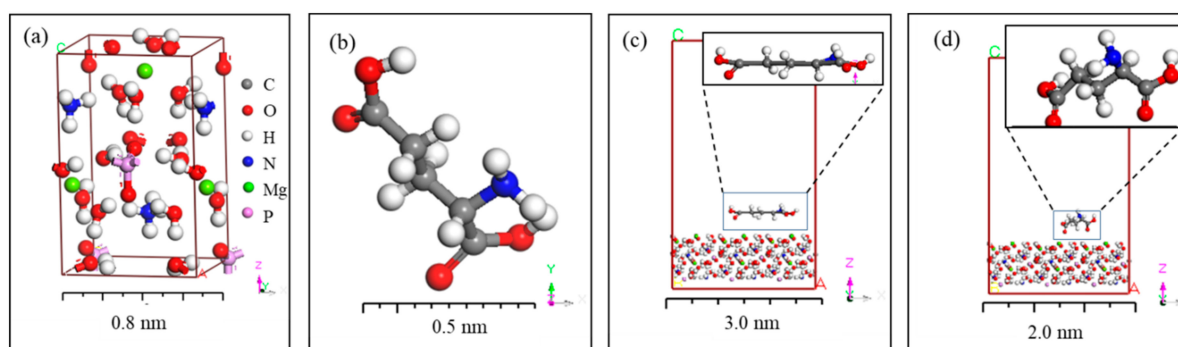


Figure 3. Molecular dynamics simulation of adsorption of Glu onto a struvite crystal: (a) 3D structure of a struvite crystal; (b) the molecular structure of Glu; (c,d) the configuration before and after adsorption of Glu onto (111) faces of struvite, respectively.

Table 2. The interaction energy between Glu and various surfaces of struvite crystals (kcal/mol).

Surfaces	011	020	111	022	002
E_{total}	6,703,266	837,073	2,007,537	6,791,561	760,446
E_{surface}	6,703,511	837,211	2,007,781	6,791,668	760,734
E_{Glu}	35.397	26.531	12.784	38.713	32.325
$E_{\text{adsorption}}$	−280.397	−164.531	−256.784	−145.713	−320.325

3.3.3. SEM and EDS Analyses of Biominerals

The morphologies and elemental composition of minerals in the experimental groups are shown in Figure 4. Minerals obtained at Mg/Ca ratio of 0 mainly have an elongate (Figure 4a) or dumbbell (Figure 4b) shape. The length of dumbbell-shaped minerals is up to 120 μm and that of elongated minerals up to 90 μm . Surfaces of these minerals are covered with small rhombohedral crystals. The main elements present are C, O, Ca, S and P (Figure 4c); S and P elements may come from EPS or the organic components of the medium. Spheroidal minerals with diameters of 10–20 μm shown in Figure 4d form clusters, and many holes were observed on these mineral surfaces (Figure 4d,e). The elements present (Figure 4f) are mainly Mg, Ca, C, O, P and S. The Mg ions come from the culture medium, and the origin of Ca, C, O, P and S is same as noted above. Figure 4g shows the irregular minerals, composed of many square crystallites with an interlacing growth pattern and sharp angles (Figure 4h). The mineral shown in Figure 4h contains C, O, Ca, Mg and P (Figure 4i). An irregular

concentric circular pattern was observed (see Figure 4j): the interior concentric minerals are composed of many larger irregular crystallites (Figure 4k), and the outer layer is mainly composed of small particles. The main elements in the mineral are C, O, Ca, Mg, S and P (Figure 4l). Prismatic struvite was obtained at Mg/Ca ratio of 12 (Figure 4m,n). The elemental composition of prismatic struvite marked with a square includes Mg, O, P, N and S (Figure 4o).

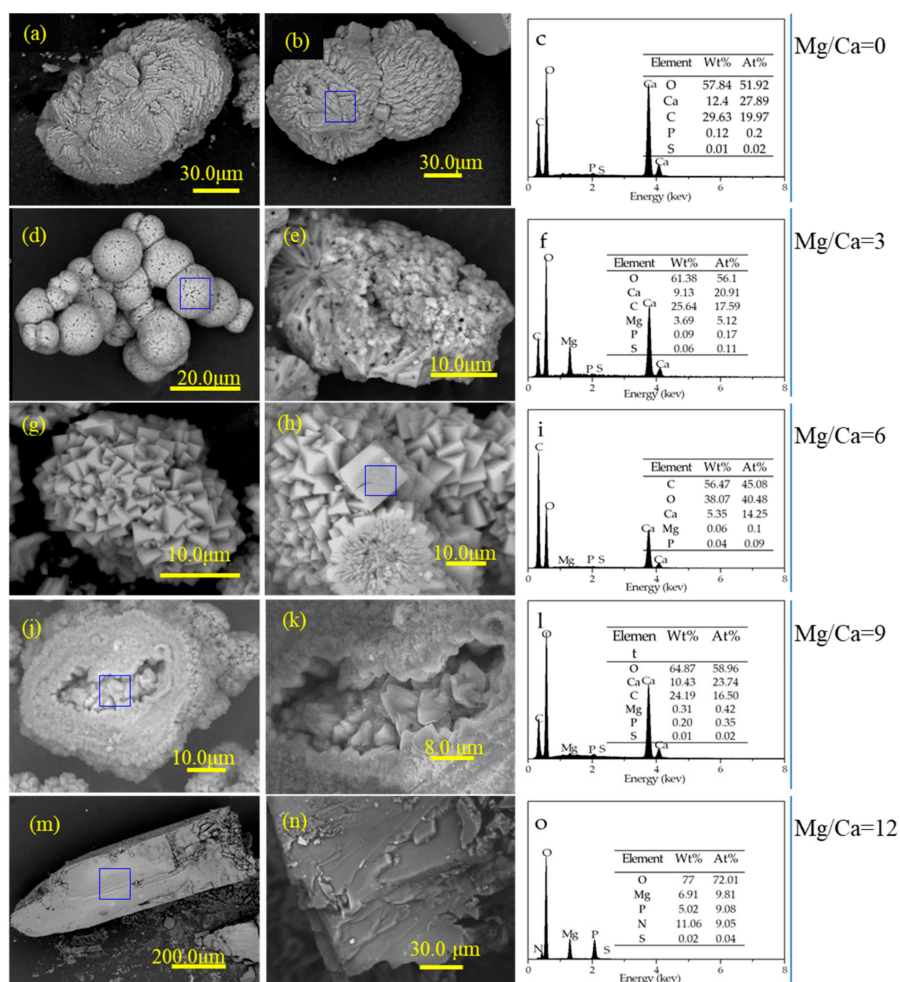


Figure 4. Scanning electron microscope (SEM) and Energy dispersive spectrum (EDS) images of minerals precipitated in the culture mediums at different Mg/Ca ratios: (a,b,d,e,g,h,j,k,m,n) are morphologies of minerals at Mg/Ca molar ratios of 0, 3, 6, 9 and 12, respectively; (c,f,i,l,o) are the EDS analyses of minerals marked by a blue square in a2, b1, c2, d1 and e1, respectively.

3.3.4. HRTEM, SAED, STEM and Elemental Mapping Analysis of the Minerals

As can be seen in the HRTEM and SAED images (Figure 5), Mg-rich calcite precipitates were ground into nanoparticles (Figure 5a). The interplanar distances, d (Å), are 2.0771, 2.2605, 2.4380, 2.8067 and 2.9465, and the corresponding crystal planes are (202), (113), (110), (006) and (104) (Figure 5b). In addition, from the SAED pattern (Figure 5c), clear diffraction spots and rings appear in the diffraction pattern of Mg-rich calcite, indicating a good crystal structure for these particles. The calculated interplanar distances, d (Å), are 1.6347, 2.3948 and 3.0998, respectively, which correspond to the crystal planes of (111), (110) and (104), respectively. These lattice distance values d (Å) are also identical to those of the standard PDF card of Mg-rich calcite (PDF#43-0697). Thus, it can be concluded that the mineral obtained at Mg/Ca molar ratio of 3 is a Mg-rich calcite.

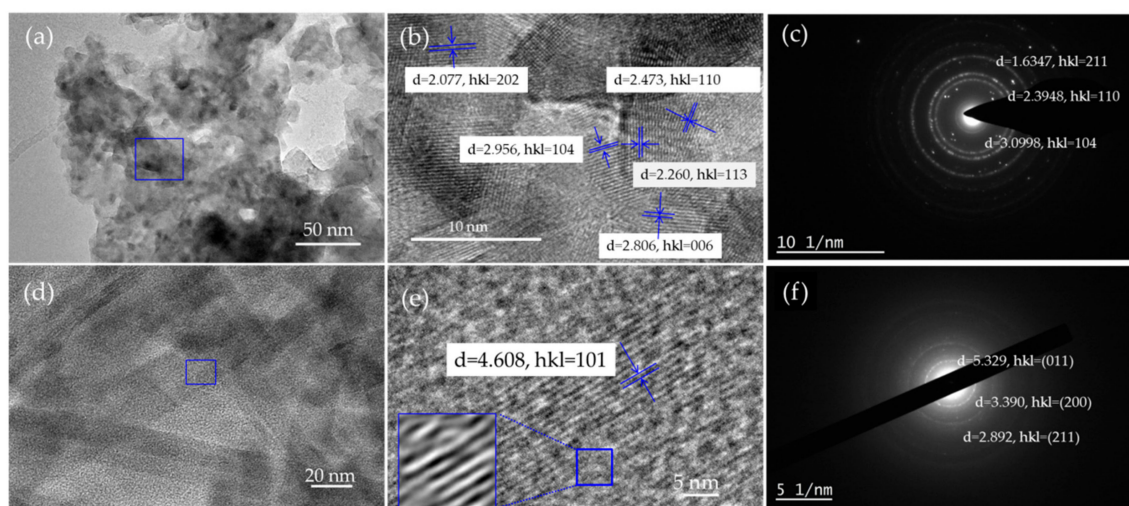


Figure 5. HRTEM and SAED results of the biotic Mg-rich calcite and struvite nanoparticles: (a) HRTEM image of Mg-rich calcite nanoparticles; (b), enlarged image of the area marked by a blue square in a; (c) SAED results corresponding to the area marked by the blue square in a; (d), HRTEM image of a struvite nanoparticle; (e), enlarged image of the area marked by a blue square in d; (f) SAED results corresponding to the area marked by a blue square in d.

From the HRTEM image (Figure 5d), it can be seen that the struvite minerals have a fibrous shape after being ground thoroughly. The interplanar distance, d (Å), is 4.6080, and the corresponding crystal plane is (101) (Figure 5e). In addition, the SAED pattern (Figure 5f) shows clear diffraction spots and rings, indicating a good crystal structure for the struvite particles. The calculated interplanar distance, d (Å), are 5.329, 3.390 and 2.892, respectively, which correspond to the crystal planes of (011), (200) and (211), respectively. These lattice distance values, d (Å), are also identical with those of the standard PDF card of struvite. Thus, it can be concluded that the mineral particles obtained at Mg/Ca molar ratio of 12 are struvite. It can be inferred that the ZW123 bacterium can affect the crystal structure of struvite. Dislocation phenomena are also obviously present (blue box in Figure 5e), which may be due to the addition of organic metabolites.

Elemental mapping of the Mg-rich calcite nanoparticles was also conducted (Figure 6). Mg-rich calcite was ground into nanoparticles (Figure 6a), and the element distribution maps of Mg and Ca (Figure 6b,c) show that Mg ions are uniformly distributed within the Mg-rich calcite nanoparticles. Thus, Mg^{2+} ions entered into the calcite lattice easily with the participation of the ZW123 bacterium. The element P was also detected in the Mg-rich calcite lattice (Figure 6d), which also indicates that P may enter into the calcite lattice and could be a factor in the formation of the Mg-rich calcite.

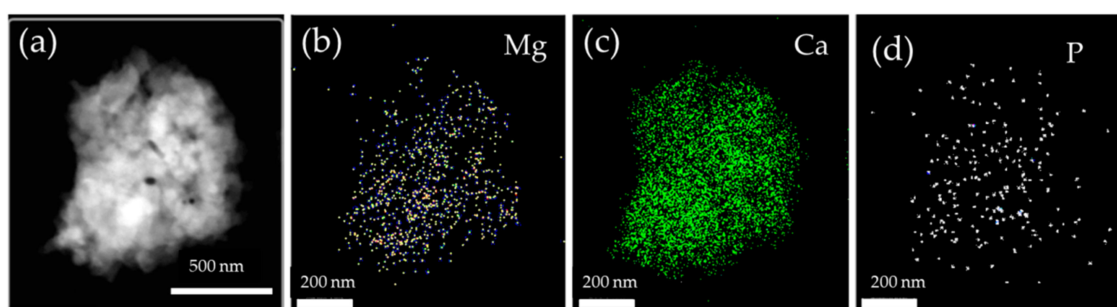


Figure 6. STEM images and elemental mapping of Mg-rich calcite: (a), image of Mg-rich calcite; (b), (c), and (d), represent the distribution of Mg, Ca and P elements, respectively, within Mg-rich calcite crystals.

3.3.5. FTIR Analyses

The adsorption peaks at 712, 875 and 1421 cm^{-1} are the characteristic peaks of calcite, and the characteristic peaks of vaterite are at 745, 870 and 1421 cm^{-1} [2,7]. In addition, the peaks at 700, 765, 872, 1064, 1401 and 1480 cm^{-1} record the presence of monohydrocalcite [7,58]. Characteristic peaks of struvite include the H–O–H group for water molecules at 1656 cm^{-1} ; the symmetrical and asymmetrical bending vibration of N–H (NH_4^+) at 1609 and 1439 cm^{-1} ; the asymmetrical stretching vibration of PO_4^{3-} at 1003.79 and 571.78 cm^{-1} ; the symmetrical bending vibration of PO_4^{3-} at 453.16 cm^{-1} ; the hydrogen bond between waters at 762.4 cm^{-1} and the hydrogen bond between ammonium and water at 886.70 cm^{-1} [22,32]. As seen from Figure 7a, adsorption peaks at 710, 870 and 1082 cm^{-1} indicate the presence of calcite at Mg/Ca ratios of 0 and 3, and the peak at 745 cm^{-1} indicates that vaterite is also present at the Mg/Ca ratio of 0. The peaks at 698, 760, 870, 1064, 1401 and 1480 cm^{-1} demonstrate that monohydrocalcite is the dominant mineral at Mg/Ca ratios of 6 and 9. The peaks at 569, 760, 889, 1003, 1439, 1602 and 1678 cm^{-1} indicate the existence of struvite at the Mg/Ca ratio of 12. Many kinds of organic functional groups, such as C–O, O–H, C–H, C=O, C–O–C and N–H were detected in EPS (Figure 7b) and these functional groups may be due to the amino acids and polysaccharides there. The FTIR spectra of supernatants, after the minerals were processed by thorough ultrasonic shaking, are identical with the distilled water (Figure 7c) [11]; this indicates that the organic substances on the mineral surfaces were removed completely. Some organic functional groups within the mineral interiors at various Mg/Ca ratios, such as C–O–C, C–O, O–H, C–H and C=O, were also detected, shown in Figure 7d; most of these organic functional groups were also detected in the EPS from the ZW123 bacterium (Figure 7b). Thus, it can be inferred that some organic matter was involved in the biomineralization process. These organic functional groups may come from the *C. freundii* ZW123 bacterium or its metabolites or the organic component of the medium.

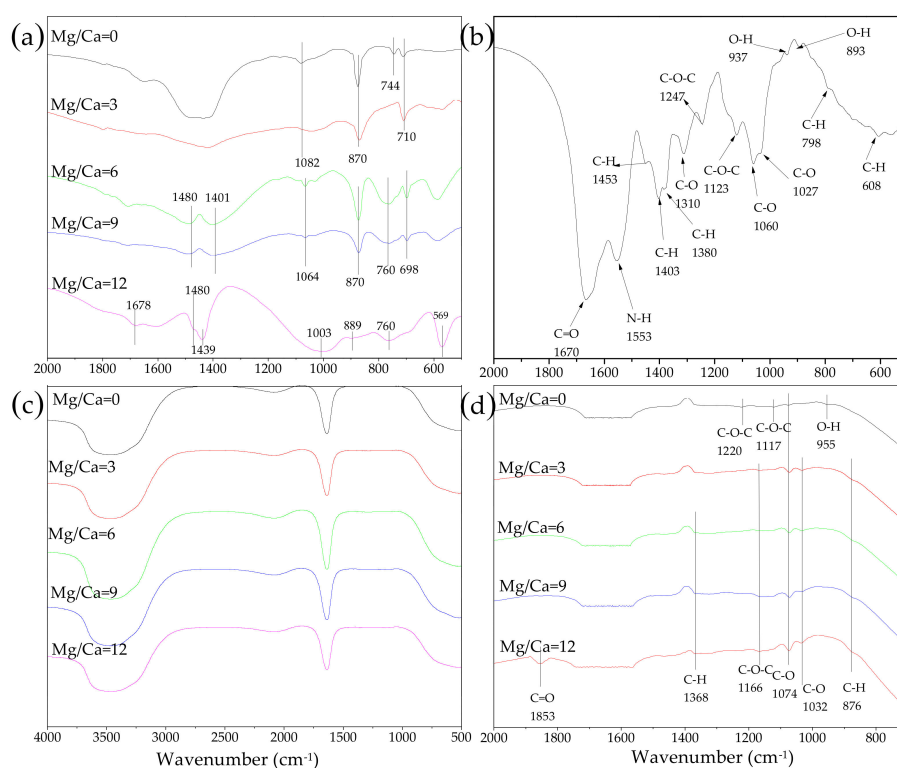


Figure 7. FTIR images of minerals precipitated in the culture mediums at different Mg/Ca ratios. (a) the FTIR patterns of biotic minerals; (b) FTIR analysis of EPS; (c) FTIR analyses of the supernatant after the minerals have been processed by thorough ultrasonic shaking; (d) FTIR analyses of the organic functional groups within minerals.

3.4. Amino Acid Composition of EPS

Sixteen kinds of amino acid were detected in EPS (Figure 8a), and the most abundant one was Glu followed by glycine (Gly), alanine (Ala) and aspartic acid (Asp). Most of the amino acids except lysine (Lys) and arginine (Arg) were negatively charged due to deprotonation (pH > 8.0). These negatively charged amino acids, especially Asp and Glu with one free carboxyl group, play a more important role in the biomineralization process because of their enhanced ability to adsorb Mg and Ca ions in the alkaline environment. The amino acid composition of organic matter within the minerals is shown in Figure 8b, which is almost the same as that of EPS, indicating that EPS play an important role in the biomineral formation process.

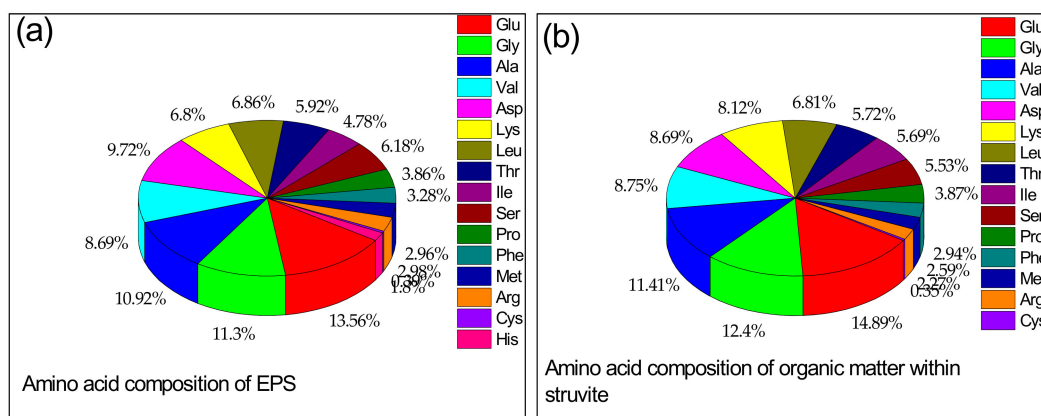


Figure 8. Amino acid composition of EPS (a) and amino acid composition of organic matter within struvite at Mg/Ca ratio of 12 (b).

The accumulation of the proline acid (Pro) is considered to be associated with the saline tolerance of microorganisms [60]. Pro can balance the osmotic pressure of cells when osmotic pressure is increased in the environment. In addition, glycine betaine is also able to protect cells from osmotic stress and maintain the osmotic balance of living cells [61]. This important role played by glycine betaine may be closely related with the protein stability and reduction of cytoplasmic ion strength. Glycine betaine can be produced through synthesis inside the cell or accumulation of exogenous additives. The synthesis of glycine betaine is one good strategy to reduce saline inhibition for the microorganism when there is not enough exogenous glycine betaine [62]. Nyssola studied a novel biosynthetic pathway for glycine betaine and found that the methylation reactions from Gly to betaine are catalyzed by two methyltransferases from two extreme halophiles. In this study, Gly and Pro were both detected within the EPS (Figure 8a), and Gly in the EPS may be transformed into glycine betaine in this biosynthetic pathway.

Therefore, accumulation of glycine betaine and Gly can improve the tolerance of microorganisms to salt [61,63]. Thus, in this study, the bacterial reproduction of ZW123 in the anaerobic saline environment may be due to the abundance of Gly and Pro in the EPS.

3.5. XPS Analyses of Biotic Struvite

XPS spectra are presented in Figure 9 and the main peaks attributed to P2p, S2s, C1s, N1s, O1s and Mg1s are evident (Figure 9a) on the XPS survey of biotic struvite. The characteristic peak of Mg1s at 1304.3 eV (Figure 9b) represents the presence of the MgOH bond [64].

The XPS N1s spectrum of the struvite crystal is shown in Figure 9c. A single symmetrical peak appeared at the binding energy of 401.3 eV, due to the presence of NH_4^+ groups [65]. The XPS P2p spectrum shows that a characteristic peak at 133.2 eV (Figure 9d), ascribed to the P=O group of struvite [66]. The XPS O1s spectrum is deconvoluted into two peaks at 530.7 eV and 532.5 eV (Figure 9e), due to the MgOH bonds and POH bonds, respectively [67]. The XPS C1s spectrum is

deconvoluted into three peaks at 284.7 eV, 286.3 eV and 288.2 eV (Figure 9f), which are attributed to C–(C, H) at 284.7 eV, C–(O, N) from amide, alcohol and ether at 286.3 eV, C=O from carboxylate, ester and carbonyl at 288.2 eV, respectively [68–70]. The XPS S2s spectrum peak is located at 166.5 eV (Figure 9g), due to the presence of organic sulfur in cysteine acid (Cys). Thus, some organic functional groups have been detected on the mineral surface, which is in good agreement with the FTIR results. This further indicates the important role that microorganisms play in the biomineral formation process.

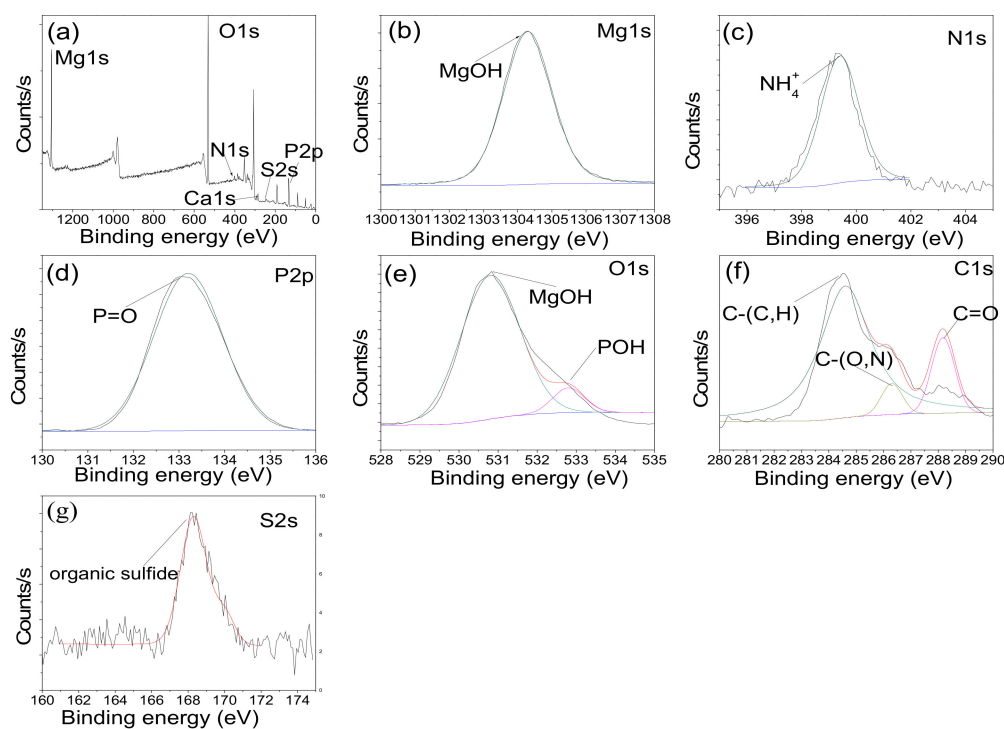


Figure 9. XPS spectra of struvite induced by the bacterium ZW123 ((a): bond survey of biotic struvite surface; (b–g): high-resolution of Mg, N, P, O, C and S, respectively).

3.6. Stable Isotope Composition of Minerals and Organic Carbon Sources

To further understand the relationship between the carbonate minerals and the microorganisms, the stable carbon isotope composition of the Ca-carbonate minerals was determined. From Table 3, the stable carbon isotope values $\delta^{13}\text{C}_{\text{PDB}}$ (‰) of biotic carbonate minerals at Mg/Ca ratios of 0, 3, 6 and 9 (−18.5~−16.8‰) are much more negative than those of abiotic minerals (abiotic calcite, −11.19 and abiotic monohydrocalcite, −11.63‰). The stable carbon isotope values $\delta^{13}\text{C}_{\text{PDB}}$ (‰) of organic substances yeast extract is −21.8‰ whereas the $\delta^{13}\text{C}_{\text{PDB}}$ (‰) values of CO_2 in the atmosphere is −8.0‰ [71]. The stable carbon isotope composition of biotic minerals is much closer to the organic substances rather than CO_2 . Thus, it can be assumed that carbon in the biotic carbonate minerals is mainly derived from the organic substances rather than the CO_2 in the atmosphere. The organic substances will be consumed to produce CO_2 through microbial metabolism, and the produced CO_2 will be converted into carbonate and bicarbonate ions through hydration reactions under the catalysis of CA; this results in the increasing supersaturation and drives the precipitation of carbonate minerals.

Table 3. Stable carbon and nitrogen isotope values of the biotic and abiotic minerals, yeast extract, and NH₄Cl.

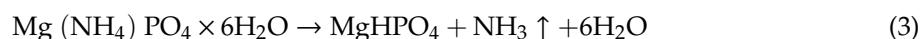
Mg/Ca Molar Ratio	Biotic Minerals			Abiotic Minerals		Yeast Extract	NH ₄ Cl	
	δ ¹³ C (‰)	δ ¹⁵ N (‰)	δ ¹⁵ N (‰)	Calcite δ ¹³ C (‰)	Monohydrocalcite δ ¹³ C (‰)	Struvite δ ¹⁵ N (‰)	δ ¹³ C (‰)	δ ¹⁵ N (‰)
0 (calcite + vaterite)	−16.8	/		−11.19				
3 (Mg-rich calcite)	−17.9	/					−21.8	
6 (Monohydrocalcite)	−18.5	/						
9 (Monohydrocalcite)	−18.5	/			−11.63			
12 (Struvite)	/	2.20	−0.35			−0.12		4.35

In this study, stable nitrogen isotope value δ¹⁵N (‰) of biotic struvite induced by the ZW123 bacterium is 2.20‰, which is more positive than that of abiotic struvite (−0.12‰) (Table 3). The stable nitrogen isotope value δ¹⁵N of organic substances (yeast extract) is 4.35‰, whereas that of inorganic nitrogen source (NH₄Cl) is −0.35‰. The stable nitrogen isotope value δ¹⁵N (‰) of biotic struvite is between those of yeast extract and NH₄Cl, which indicates that nitrogen elements in the biotic struvite came from not only NH₄Cl but also the yeast extract. NH₃ is also produced in the degradation process of organic substances in the culture medium through the microbial metabolism. Released NH₃ can not only lead to an increase in pH [33] but also be involved in the formation of struvite as one of the components [29,58], which is necessary for the mineral precipitation. The stable isotope studies further emphasize the important role that microorganisms play in the bio-precipitation process of biotic minerals.

3.7. Thermal Characteristics of Biotic and Abiotic Struvite

The TG, DTG, and DSC curves of abiotic and biotic struvite at a heating rate of 10 °C per minute are shown in Figure 10. TG analyses are usually used to evaluate the existence, thermal stability and decomposition characteristics of volatile components.

As seen from the TG curves (Figure 10a), the thermal stability of biotic struvite induced by bacteria records a weight loss from room temperature to 180 °C; this would be due to the evaporation of water molecules and ammonia according to the following Equation (3). The continuous weight loss is due to the release of one mole of ammonia and six moles of water molecules through ammonium decomposition and dehydration reactions. The weight percent of ammonia in the standard struvite is 6.94% and the weight percent of water molecules is 44.04%; thus, the theoretical total weight loss is 50.98%, which is somewhat lower than the total weight loss in our result (54.4%):



The DTG analysis shows a sharp peak at 116 °C in Figure 10c (the enlarged figure of Figure 10b), which may be attributed to the elimination of crystal water and ammonia molecules. At this point, the decomposition rate reached the maximum. The DSC result for struvite is also present in Figure 10d; one main peak at 118 °C is observed and this endothermic peak is due to the dehydration of crystalline water molecules and ammonia in the struvite decomposition process (Equation (3)). Another exothermic peak at around 688 °C is due to the transformation from MgHPO₄ to pyrophosphate (Mg₂P₂O₇) (Equation (4)):



The differences between abiotic and biotic struvite are clearly observed. The decomposition temperature of biotic struvite is higher than that of abiotic struvite (Figure 10b,c), indicating the enhanced thermal stability and better crystallinity of biotic struvite. In addition, the enthalpy change (ΔH) of biotic struvite is higher than that of abiotic struvite (Figure 10d), which also confirms our assumption that the thermostability should increase and crystallinity should improve with the participation of the ZW123 bacterium.

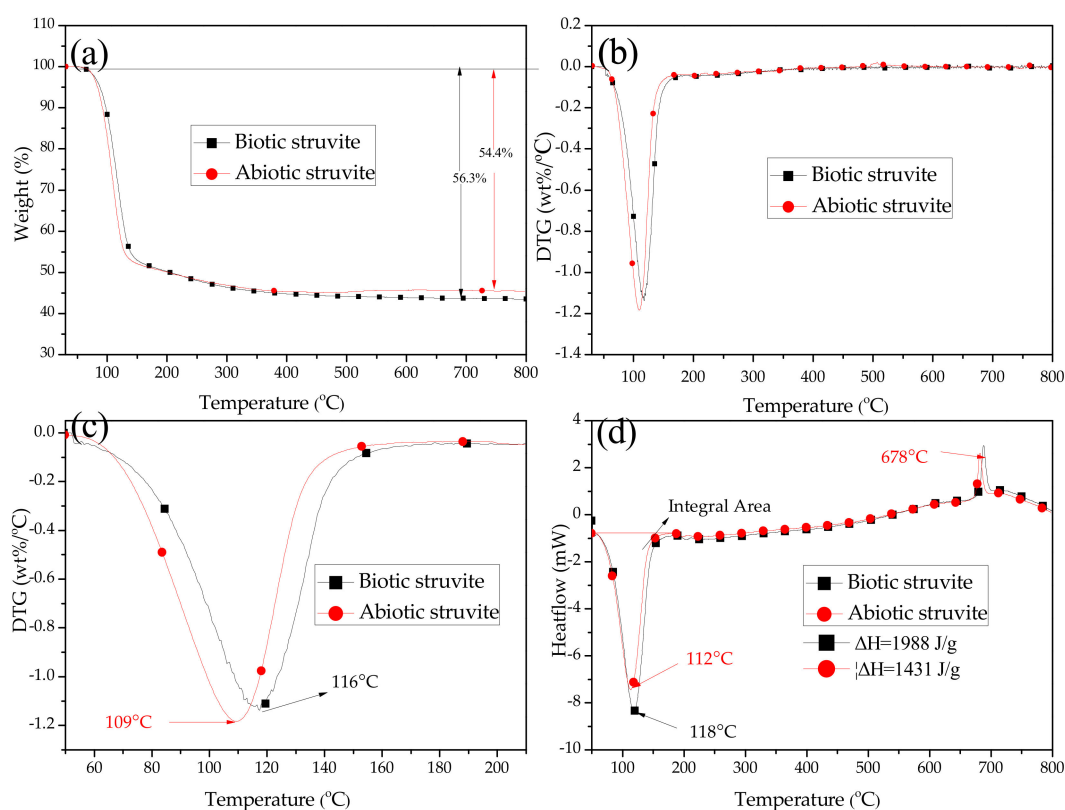
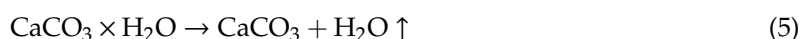


Figure 10. TG (a), DTG (b,c) and DSC (d) analyses of struvite induced by the bacterium ZW123.

Thermal stability characteristics of monohydrocalcite at Mg/Ca ratios of 6 and 9 were also investigated and results are shown in Figure 11. As can be seen in the TG curve (Figure 11a), the decomposition of monohydrocalcite occurred mainly in two periods. The first weight loss period is due to the loss of crystal water (Equation (5)), and the second loss period is mainly attributed to the release of carbon dioxide (Equation (6)):



The thermal decomposition temperature reached the maximum at 758 °C for the monohydrocalcite at Mg/Ca ratio of 9 (Figure 11b), which is lower than that for the Mg/Ca ratio of 6 (774 °C), indicating that thermal stability decreased with increasing Mg/Ca molar ratios.

DSC results show that the enthalpy change (ΔH) of monohydrocalcite at Mg/Ca ratio of 6 is 195.22 J/g (Figure 11c), which means 195.22 J of energy was needed in the thermal decomposition process of 1 g of monohydrocalcite. Much more energy was needed for the thermal decomposition of monohydrocalcite at Mg/Ca ratio of 6 (195.22 J/g), than that at Mg/Ca ratio of 9 (171.92 J/g) (Figure 11c), indicating that monohydrocalcite at Mg/Ca ratio of 6 had a higher thermal stability than that at Mg/Ca ratio of 9. This phenomenon may be due to the better crystallinity of monohydrocalcite at the Mg/Ca ratio of 6, which is consistent with the XRD results (Table 1). Thus, it can be inferred that more magnesium ions may enter into the crystal lattice and affect the crystallinity of monohydrocalcite when the Mg/Ca molar ratio increases.

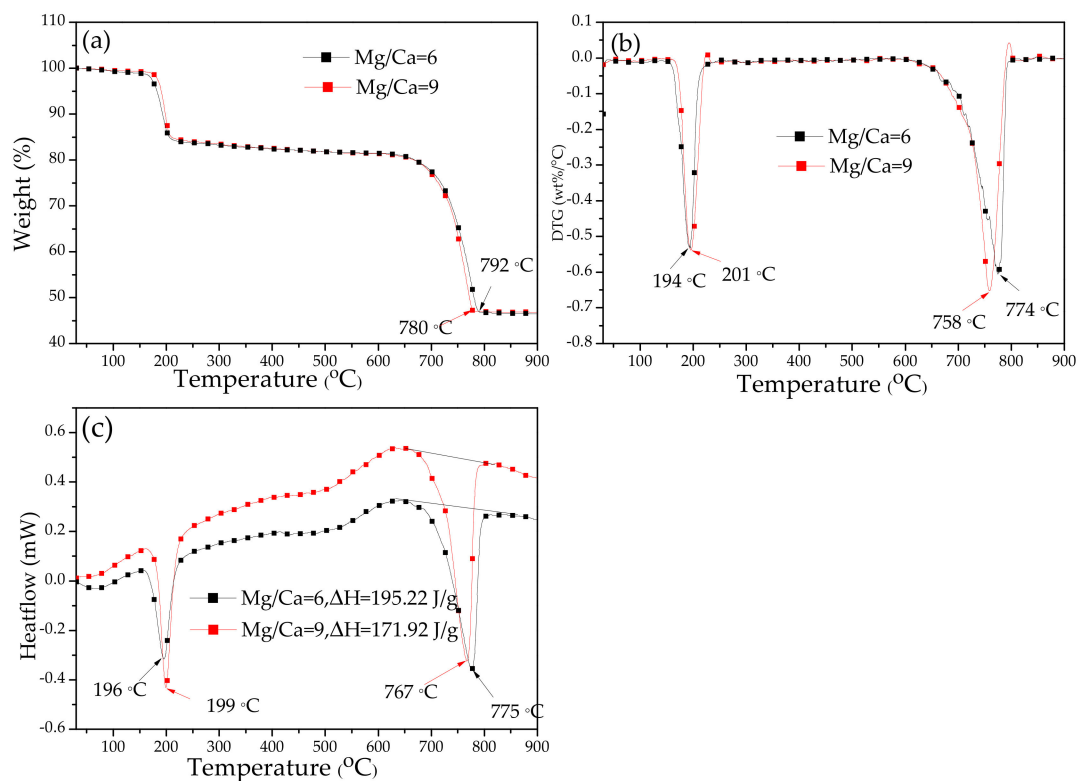


Figure 11. TG (a), DTG (b), DSC (c) of monohydrocalcite at Mg/Ca molar ratios of 6 and 9.

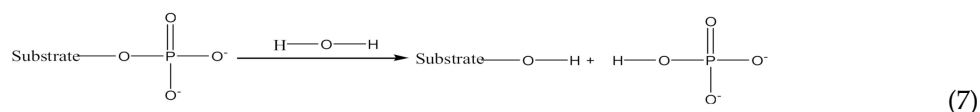
4. Discussion

4.1. Physiological and Biochemical Parameters and the Favourable Environment for Biomineralization

Many researchers have demonstrated that microorganisms, especially bacteria, can provide a favorable environment for the biomineralization of carbonate and phosphate minerals [3,4,21,28,32]. Carbonate and phosphate minerals are usually formed when supersaturation is reached in an alkaline environment [22,71]. The bioprecipitation of carbonate and phosphate minerals induced by the ZW123 bacterium in an anaerobic laboratory environment has rarely been reported. Our results indicate that the ZW123 bacterium played a significant role in the mineral precipitation process on the basis of the distinctive mineralogies, precipitate morphologies, organic functional groups, stable isotope values and thermal stability characteristics [7,22]. The absence of minerals in the control group inoculated with sterile distilled water further strengthens our interpretations.

Bacterial metabolic activities play an important role in the bioprecipitation process of carbonate minerals, for instance, it results in the changes in pH, ionic strength and ionic composition, and affects the cell-surface charges [28]. In this study, pH in the experimental group inoculated with ZW123 bacterium reached 8.02, whereas pH was almost unchanged in the control group without inoculation of bacterium; this difference is likely related to the metabolic activities of *C. freundii* ZW123. Ammonia released by bacteria has been reported to play an important role in pH increase in the previous studies [28]; however, many researchers have proposed that other factors could also result in a pH increase. Zhuang et al. ascribed the increase in pH to the combined effect of ammonia and CA [7]. CA can catalyze the hydration reaction of carbon dioxide to generate bicarbonate and carbonate ions, further increasing the pH in the medium. In this study, bicarbonate and carbonate concentrations were determined and the pH changes were also measured. The pH based on bicarbonate and carbonate was higher than the pH in the experimental group; thus, CA can also promote a pH increase.

The pattern of ALP activity was almost consistent with that of the bacterial growth, and ALP can catalyze the breakage of phosphate ester bonds to contribute to the removal of phosphate group from substrate molecules, resulting in the production of phosphate ions (Equation (7)):



The presence of phosphate ions could lead to the deprotonation of water molecules, so releasing hydroxyl groups, and resulting in an increase in pH and alkalinity. Thus, the pH increase in the experimental groups was mainly due to the combined effects of ammonia, CA and ALP. Alkaline environments are favorable for the biomineralization of carbonate and phosphate minerals. Bicarbonate and carbonate ions can be produced through the hydration of carbon dioxide under the catalytic reaction of CA, and this would increase supersaturation and promote the precipitation of carbonate minerals in the induction medium. Thus, carbonate minerals in this study were precipitated according to the following Equation (8):



Struvite is considered the product of bioprecipitation through the chemical reaction of ammonium, magnesium and phosphate ions [22]. The suitable alkaline environment for struvite precipitation was likely obtained through bacterial metabolism. Ammonium and phosphate ions were provided by the medium composition and bacterial metabolites, and the supersaturation for struvite was then reached. Reaching supersaturation is a key step in the biomineralization process [22]. Struvite was precipitated according to the following Equation (9):



These results reveal the formation mechanism of carbonate and phosphate minerals induced by *C. freundii* ZW123, including the adsorption of Ca^{2+} and Mg^{2+} on to cell surfaces, and the production of carbonate, phosphate and ammonium ions during bacterial metabolization. Thus, microorganisms play an important role in the biomineralization processes of carbonate and phosphate minerals.

4.2. Magnesium Content in Biotic Mg-Rich Calcite

The magnesium content of bio-mediated carbonates is often used as an indicator of climatic conditions and palaeotemperature [72,73]. It is generally believed that magnesium ions can enter the calcite lattice because magnesium ions are smaller in diameter than calcium ions, leading to the formation of Mg-rich calcite. The content of magnesium in magnesian calcite formed under inorganic conditions at room temperature is about 6% (molar percent); however, the magnesium content in biogenic magnesian calcite is the range of 20–45% (molar percent) in many marine organisms, such as calcareous red algae, echinoids, starfish and some foraminifera [74,75]. In this study, magnesium content was above 10% (molar percent, Figure 4, Figure 7), and this high magnesium content may also be closely related with the *C. freundii* ZW123 bacterium.

Previous studies have shown that organic matter plays an important role in regulating the content of magnesium in biogenic magnesian calcite [74,75]. Robach et al. studied echinoid teeth which were composed of Mg-rich calcite, and recorded the distribution map of Mg, Ca and mineral-related proteins; they also found that there was a strong correlation of Asp residue and Mg-rich calcite, indicating that Asp may be closely related to the formation of the Mg-rich calcite [75]. Stephenson et al. investigated the magnesium content in calcite mediated by peptide, and found that magnesium content increased by 50–75% compared to inorganic conditions [72], which may be due to the stronger dehydration of magnesium ions in the presence of peptide.

In our opinion, these organic substances may control the magnesium content in magnesian calcite. It is well known that the dehydration of hydrated Mg^{2+} ion with six water molecules ($[Mg(H_2O)_6]^{2+}$) is difficult, and the energy needed for the dehydration of ($[Mg(H_2O)_6]^{2+}$) is much higher than that of $[Ca(H_2O)_6]^{2+}$ [3]. Past studies have found that the water molecules in the hydrated Mg^{2+} ion can be replaced by carboxyl group [76]; once one water molecule is replaced by a carboxyl group, the dehydration of other water molecules will become easier. In this study, the amino acid composition of EPS (Figure 8) shows that EPS contain large amounts of Asp and Glu with free carboxyl groups. Thus, Asp and Glu may contribute to the dehydration of $[Mg(H_2O)_6]^{2+}$, facilitating the formation of free magnesium ions and reducing the energy barrier for magnesium ions to enter the calcite crystal lattice. Thus, Asp and Glu may also contribute to the high magnesium content of Mg-rich calcite.

4.3. The Role of Magnesium Ions in Monohydrocalcite Formation

Monohydrocalcite is a metastable carbonate mineral compared with calcite and aragonite, which makes it rare in natural environments. It has been reported that the formation of monohydrocalcite always needs a high Mg/Ca ratio [77,78]; thus, much more attention has been paid to the important role played by magnesium ions in the formation process of monohydrocalcite [29]. Dejehet et al. reported that monohydrocalcite spheroids were surrounded with a high-magnesium content layer, and this layer enhanced the stability of monohydrocalcite [79]. In addition, hydrous magnesium carbonate (e.g., nesquehonite) and monohydrocalcite have been reported in lake sediments of the East Basin Lake and Lake Manito, Canada [80], where the formation and stabilization of these minerals was attributed to the high concentration of magnesium ions and hydrous magnesium carbonate. Rodriguez-Blanco et al. proposed that monohydrocalcite could be transformed from amorphous calcium carbonate (ACC), and then into more stable calcium carbonate phases (e.g., calcite and aragonite) without the presence of magnesium [81]. In this study, monohydrocalcite persisted and was not transformed into other more stable phases. Thus, it can be inferred that maybe the presence of magnesium ions maintains the stability of monohydrocalcite and prevents it from transforming into more stable anhydrous calcium carbonate. Magnesium ions within the ACC structure apparently can slow or halt the dehydration, and ACC will be transformed into the hydrated calcium carbonate in the presence of hydrous magnesium [81]. Monohydrocalcite formed via an ACC phase must be surrounded by hydrous magnesium, which prevents the transformation from monohydrocalcite to a more stable anhydrous calcium carbonate phase. In our study, magnesium in the medium plays the same role in maintaining the stability of monohydrocalcite. It has been reported that a higher Mg/Ca molar ratio in the culture medium is a prerequisite for the formation of monohydrocalcite. According to the previous study of monohydrocalcite [81], Mg/(Mg + Ca) ratio of 0.3 was high enough to form monohydrocalcite, whereas in our study, the Mg/Ca ratio of 3 was not high enough to form monohydrocalcite. This difference may be due to the particular culture conditions and the different sources of Mg^{2+} ions, which needs to be further studied.

4.4. Struvite Induced by *C. freundii* ZW123

Microorganisms play an important role in biomineralization processes in many environments, and the bio-precipitation of different carbonate minerals induced by different species of bacteria has been widely reported [5,12,13,71,82]. However, investigations of struvite and its geological significance have rarely been reported due to the scarcity of struvite in natural environments and ancient rocks. In the natural environment, struvite is less stable and easily transforms into other mineral phases. In fact, struvite only persists in an environment with abundant organic substances, such as guano deposits, old cemeteries and urinary facilities [28,83]. Thus, struvite precipitation has usually been associated with microorganisms, especially bacteria, and the presence of diverse organic metabolites released by the microorganisms. In this study, EPS, consisting of complex organic metabolites, may maintain the stability of struvite and prevent it from transforming into other minerals. According to crystallization kinetics, the formation of struvite crystals can be divided into two stages: a nucleation

stage and a crystal growth stage. It is universally accepted that microorganisms can provide nucleation sites for bacterially-induced mineral precipitation [7,16,17,24]. Negatively-charged amino acids in EPS, for instance, Glu and Asp, can adsorb magnesium ions and create a supersaturated microenvironment. Thus, bacterial EPS may serve as the nucleation sites in the nucleation stage [7]. In this study, organic functional groups within struvite crystals were detected, and in addition, the amino acid composition of the organic substances within the struvite was almost identical with that of EPS. These findings demonstrate that EPS may play an important role in providing the nucleation sites.

It would be difficult for the precipitation of struvite when calcium ions are present in the medium, due to the fact that sulfate could react with Ca^{2+} ions to form calcium sulfate precipitates [84]. In our opinion, this inhibition effect of Ca^{2+} ions on the precipitation of struvite could be overcome by the participation of the ZW123 bacterium. Calcium ions are adsorbed on the negatively-charged EPS much easier than magnesium ions due to its ionic selectivity [26]. Carbonate ions react with calcium ions to form carbonate minerals more easily than magnesium ions. Thus, more magnesium ions could remain in the fluid to form struvite. The relatively increased and high Mg/Ca molar ratios favor the nucleation of struvite, which confirms our hypothesis that bacteria could overcome the inhibition of calcium ions on struvite precipitation.

4.5. Morphology of Struvite Induced by ZW123 Bacterium

Various morphologies of struvite induced by different microorganisms have been widely reported, including polyhedra, pseudopolyhedra and branching shapes, a granular structure, x-shape, coffin shape, arrow shape, needle shape, and radial aggregates of fine grains [15,22,85]; struvite induced by the ZW123 bacterium is mainly prism-shaped in this study. In our opinion, the variety of struvite morphologies may be due to the diverse growth rates of each crystal surface, which may be caused by the organic metabolites released by the microorganisms. Downey et al. studied the inhibition effect of acetohydroxamic acid on struvite formation, and the results indicated that struvite crystals grew rapidly along their 100-axis, forming “x-shaped” or dendritic crystals in the absence of acetohydroxamic acid; however, the growth rate of crystals declined significantly and the crystals showed an octahedral crystal habit in the presence of acetohydroxamic acid [85]. In another study [86], phosphorus citrate had a strong adsorption capacity for struvite (101) faces, leading to the changes of each crystal face and the formation of a particular arrow-shaped struvite. However, no similar changes were observed in the presence of the same concentrations of citric acid or n-sulfonic acid, which indicated the unique characteristics of phosphorous citrate in controlling the morphology of struvite. Polyaspartic acid (PASP) was once also used as a model peptide to study the effect of protein on struvite crystal morphology [87], and the results showed that arrow-shaped crystals were formed and further evolved into x-shaped and tabular-shaped structures due to the selective adsorption of PASP on the crystal faces (010), (101) and (011). In our study, the amino acid composition of organic matter within the struvite (Figure 9) was almost identical to the amino acid composition of EPS, and these amino acids may also have controlled the shape and morphology of the struvite.

Many studies have shown that organic functional groups can have a great influence on the morphologies of struvite [88]. For instance, C–O–C of organic substances may form hydrogen bonds with the hydroxyl group on the struvite surface [88]. In addition, the carboxylic group (–COOH) may combine with Mg^{2+} on the struvite surface or form hydrogen bonds with H_2O , PO_4^{3-} and hydroxyl group [85]. These interactions between organic functional groups and struvite crystals could change the growth rates of the various crystal faces, resulting in changes of morphology of the struvite. In our study, organic functional groups such as C=O, C–H and C–O–C were detected within the struvite interior according to the FTIR and XPS results (Figures 7d and 9), and these organic functional groups were also detected in the EPS (Figure 7). These organic functional groups may exert a control on struvite morphology. Hence, we propose that EPS released by the ZW123 bacterium can regulate the shape and morphology of the struvite crystals.

Many researchers have hypothesized that the morphological diversity of struvite crystals is caused by the preferential adsorption of organic matter on to different crystal surfaces. However, molecular dynamics simulation of adsorption of organic substances on to the various struvite surfaces has rarely been reported. Therefore, molecular dynamics simulation of EPS on to struvite surfaces and quantifying its adsorption energy on different crystal faces were conducted in this study in order to further understand the adsorption mechanism and to explain the morphological changes. In view of the complex composition and structural uncertainty of EPS, Glu, the most abundant amino acid in the EPS and within the minerals, was chosen as a substitute for EPS in the simulation project. We assumed that Glu could control the shape of biotic struvite to some extent.

The simulation results (Table 2) show clearly that adsorption energies of Glu to different crystal surfaces are different. Glu can inhibit the growth of crystal faces [87], and its inhibition effects on different crystal faces are diverse. Thus, the growth rates of the various crystal faces differ greatly, resulting in the morphological changes compared with chemical synthetic struvite. There are many other kinds of amino acids in the EPS in addition to Glu, and whether other amino acids can control the morphology of struvite is not clear and needs to be further studied.

4.6. Ecological Implications

Research into biomineralization of carbonate and phosphate minerals not only has scientific value but also has practical applications in several areas [28]. At present society is faced with a phosphorus supply crisis caused by overexploitation of phosphate ores and the non-renewability of phosphorus resources. At the same time, there are issues of eutrophication caused by the low utilization rate of phosphorus. In order to solve these problems, it is necessary to improve the discharge standards of nitrogen and phosphorus into wastewater and instigate the efficient recovery of phosphorus. The recovery of phosphorus from sludge by struvite precipitation could avoid the eutrophication of water. At the same time, the recovered struvite could act as a kind of slow-release fertilizer, which would be beneficial to agriculture, thus effectively offsetting the shortage of phosphorus. Industrial wastewater usually contains a high concentration of ammonia, nitrogen and phosphorus, with a Mg: P molar ratio that is relatively low; thus, it is necessary to add additional Mg ions to wastewater to produce struvite. The cost of adding magnesium for water treatment accounts for about 75% of the total cost, and this would greatly increase the cost of recovering struvite crystals. The addition of sodium hydroxide to adjust pH is also one of the major reagent costs, which greatly limits the application of this process [28,83]. In contrast, microbial metabolic activity could provide the necessary alkaline environment and create a supersaturated microenvironment for struvite precipitation around the bacteria, which would further promote the biomineralization of struvite [82]. Thus, the recovery of phosphorus by microbially-induced struvite is regarded as one potential strategy with good prospects.

Anaerobic microbial treatment technology in modern industrial wastewater treatment has been applied widely and has the prospect for lowering costs and energy consumption. In the future, more investigations of the application of anaerobic biotechnology in industrial wastewater treatment need to be conducted. Sludge anaerobic digester and its dehydrating filtrate contain high phosphate concentrations, and this is one of the best mother liquors for phosphorus recovery [35]. The metabolic activities of anaerobic bacteria like ZW123 can transform organic nitrogen and phosphorus into inorganic nitrogen and phosphorus in the form of struvite. Therefore, organic nitrogen and phosphorus can also be recovered from wastewater by the bacterially-mediated struvite precipitation method. Thus, one can conclude that the bio-precipitation of struvite in anaerobic environments is a promising strategy for wastewater treatment.

5. Conclusions

This article investigated the biomineralization of carbonate and phosphate (struvite) minerals induced by *C. freundii* ZW123 isolated from marine sediments in the Tangdao Bay (Qingdao, China). Bacterial metabolites released by the ZW123 bacterium, ammonia, CA and ALP, can result in an

increase in pH and the supersaturation of minerals. Most of the amino acids of the EPS are negatively charged and adsorb calcium and magnesium ions easily. Many organic functional groups were detected within the minerals, and the shapes and morphologies of minerals may be controlled by these organic substances to some extent. The better crystallinity of the biotic struvite also indicates that bacteria played an important role in the struvite formation process. The bacterium plays a significant role in the bio-precipitation process of carbonate and phosphate minerals in anaerobic environments and this study offers some insights into the biomineralization mechanisms of minerals and provides a promising strategy for the recovery of calcium, magnesium, ammonium and phosphate ions.

Supplementary Materials: The following are available online at <http://www.mdpi.com/2075-163X/10/1/65/s1>, Table S1: Parameter settings of molecular dynamic simulation for adsorption of Glu onto various struvite surfaces, Table S2: Physiological and biochemical identification of ZW123 and *Citrobacter freundii* species, Figure S1: Phylogenetic tree of *Citrobacter freundii* ZW123 based on the sequence alignment, Figure S2: SEM image of *Citrobacter freundii* ZW123 bacteria (a) and Gram staining test (b) and NH₃ test (c: before adding the Nessler's reagent; d: after adding the Nessler's reagent. 1, control group; 2 and 3, experimental groups), Figure S3: Rietveld refinement of XRD data at Mg/Ca molar ratio 0 (a), 3 (b), 6 (c), 9 (d) and 12 (e), Figure S4: Molecular dynamics simulation of adsorption of Glu onto crystal: a: temperature fluctuation of the adsorption of Glu onto (111) faces, b: energy fluctuation of the adsorption of Glu onto (111) face.

Author Contributions: Z.H. conceived and designed the experiments; B.S. performed the experiments; Z.H., H.Z., Y.Z. and H.Y. analyzed the results of all the experiments; B.S. and H.Y. wrote the paper; H.Z. and M.E.T. revised the manuscript. All authors have read and agreed to the published version of the manuscript.

Funding: This work was supported by the National Natural Science Foundation of China (41972108, 41772095, U1663201, 41702131); the Laboratory for Marine Mineral Resources, Qingdao National Laboratory for Marine Science and Technology (MMRZZ201804); Taishan Scholar Talent Team Support Plan for Advanced & Unique Discipline Areas, Major Scientific and Technological Innovation Projects of Shandong Province (2017CXGC1602, 2017CXGC1603); SDUST Research Fund (2015TDJH101); Natural Science Foundation of Shandong Province (ZR2019MD027, ZR2017BD001); Major Innovation Projects of Key R&D Program of Shandong Province (No.2019JZZY020808); the Scientific and Technological Innovation Project Financially Supported by Qingdao National Laboratory for Marine Science and Technology (2016ASKJ13); Open Fund of the Key Laboratory of Marine Geology and Environment, Chinese Academy of Sciences (MGE2016KG10); Level B of the SDUST Elite Scheme; Program for Graduate Science and Technology Innovation of Shandong University of Science and Technology under grant (201810424074, No.2333).

Conflicts of Interest: The authors declare no conflict of interest.

References

- Dong, H.; Fredrickson, J.K.; Kennedy, D.W.; Zachara, J.M.; Kukkadapu, R.K.; Onstott, T.C. Mineral transformations associated with the microbial reduction of magnetite. *Chem. Geol.* **2000**, *169*, 299–318. [[CrossRef](#)]
- Li, H.; Yao, Q.-Z.; Wang, F.-P.; Huang, Y.-R.; Fu, S.-Q.; Zhou, G.-T. Insights into the formation mechanism of vaterite mediated by a deep-sea bacterium *Shewanella piezotolerans* WP3. *Geochim. Cosmochim. Acta* **2018**, *256*, 35–48. [[CrossRef](#)]
- Qiu, X.; Wang, H.; Yao, Y.; Duan, Y. High salinity facilitates dolomite precipitation mediated by *Haloferax volcanii* DS52. *Earth Planet. Sci. Lett.* **2017**, *472*, 197–205. [[CrossRef](#)]
- Deng, S.; Dong, H.; Lv, G.; Jiang, H.; Yu, B.; Bishop, M. Microbial dolomite precipitation using sulfate reducing and halophilic bacteria: Results from Qinghai Lake, Tibetan Plateau, NW China. *Chem. Geol.* **2010**, *278*, 151–159. [[CrossRef](#)]
- Wang, H.; Zeng, C.; Liu, Q.; Liu, D.; Xuan, Q.; Gong, L. Calcium carbonate precipitation induced by a bacterium strain isolated from an oligotrophic cave in Central China. *Front. Earth Sci. China* **2010**, *4*, 148–151. [[CrossRef](#)]
- Han, Z.; Zhao, Y.; Yan, H.; Zhao, H.; Han, M.; Sun, B.; Meng, R.; Zhuang, D.; Li, D.; Gao, W.; et al. The Characterization of Intracellular and Extracellular Biomineralization Induced by *Synechocystis* sp. PCC6803 Cultured under Low Mg/Ca Ratios Conditions. *Geomicrobiol. J.* **2017**, *34*, 362–373. [[CrossRef](#)]
- Zhuang, D.; Yan, H.; Tucker, M.E.; Zhao, H.; Han, Z.; Zhao, Y.; Sun, B.; Li, D.; Pan, J.; Zhao, Y.; et al. Calcite precipitation induced by *Bacillus cereus* MRR2 cultured at different Ca²⁺ concentrations: Further insights into biotic and abiotic calcite. *Chem. Geol.* **2018**, *500*, 64–87. [[CrossRef](#)]

8. Couradeau, E.; Benzerara, K.; Gérard, E.; Moreira, D.; Bernard, S.; Brown, G.; Lopez-Garcia, P. An early-branching microbialite cyanobacterium forms intracellular carbonates. *Science* **2012**, *336*, 459–462. [[CrossRef](#)]
9. Kajiyama, S.; Nishimura, T.; Sakamoto, T.; Kato, T. Aragonite nanorods in calcium carbonate/polymer hybrids formed through self-organization processes from amorphous calcium carbonate solution. *Small* **2014**, *10*. [[CrossRef](#)]
10. Kim, H.J.; Shin, B.; Lee, Y.S.; Park, W. Modulation of calcium carbonate precipitation by exopolysaccharide in *Bacillus* sp. JH7. *Appl. Microbiol. Biotechnol.* **2017**, *101*, 6551–6561. [[CrossRef](#)] [[PubMed](#)]
11. Pan, J.; Zhao, H.; Tucker, M.E.; Zhou, J.; Jiang, M.; Wang, Y.; Zhao, Y.; Sun, B.; Han, Z.; Yan, H. Biomineralization of monohydrocalcite induced by the halophile *Halomonas smyrnensis* WMS-3. *Minerals* **2019**, *9*, 632. [[CrossRef](#)]
12. Qiu, X.; Yao, Y.; Wang, H.; Shen, A.; Zhang, J. Halophilic archaea mediate the formation of proto-dolomite in solutions with various sulfate concentrations and salinities. *Front. Microbiol.* **2019**, *10*, 480. [[CrossRef](#)] [[PubMed](#)]
13. Lian, B.; Hu, Q.; Chen, J.; Ji, J.; Teng, H.H. Carbonate biomineralization induced by soil bacterium *Bacillus megaterium*. *Geochim. Cosmochim. Acta* **2006**, *70*, 5522–5535. [[CrossRef](#)]
14. Zhou, G.-T.; Yao, Q.Z.; Ni, J.; Jin, G. Formation of aragonite mesocrystals and implication for biomineralization. *Am. Mineral.* **2009**, *94*, 293–302. [[CrossRef](#)]
15. Han, Z.; Zhao, Y.; Yan, H.; Zhao, H.; Han, M.; Sun, B.; Sun, X.; Hou, F.; Sun, H.; Han, L.; et al. Struvite precipitation induced by a novel Sulfate-Reducing Bacterium *Acinetobacter calcoaceticus* SRB4 isolated from river sediment. *Geomicrobiol. J.* **2015**, *32*, 868–877. [[CrossRef](#)]
16. Yan, H.; Han, Z.; Zhao, H.; Zhou, S.; Chi, N.; Han, M.; Kou, X. Characterization of calcium deposition induced by *Synechocystis* sp. PCC6803 in BG11 culture medium. *Chin. J. Oceanol. Limn.* **2014**, *32*, 503–510. [[CrossRef](#)]
17. Han, Z.; Meng, R.; Yan, H.; Zhao, H.; Han, M.; Zhao, Y.; Sun, B.; Sun, Y.; Wang, J.; Zhuang, D.; et al. Calcium carbonate precipitation by *Synechocystis* sp. PCC6803 at different Mg/Ca molar ratios under the laboratory condition. *Carbonates Evaporites* **2017**, *32*, 561–575. [[CrossRef](#)]
18. Han, Z.; Yan, H.; Zhao, H.; Zhou, S.; Han, M.; Meng, X.; Zhang, Y.; Zhao, Y.; Sun, B.; Yao, C.; et al. Bio-precipitation of calcite with preferential orientation induced by *Synechocystis* sp. PCC6803. *Geomicrobiol. J.* **2014**, *31*, 884–899. [[CrossRef](#)]
19. Han, Z.; Yan, H.; Zhou, S.; Zhao, H.; Zhang, Y.; Zhang, N.; Yao, C.; Zhao, L.; Han, C. Precipitation of calcite induced by *Synechocystis* sp. PCC6803. *World J. Microbiol. Biotechnol.* **2013**, *29*, 1801–1811. [[CrossRef](#)]
20. Vasconcelos, C. Microbial mediation of modern dolomite precipitation and diagenesis under anoxic conditions (Lagoa Vermelha, Rio de Janeiro, Brazil). *J. Sediment. Res.* **1997**, *67*. [[CrossRef](#)]
21. Warthmann, R.; Lith, Y.; Vasconcelos, C.; McKenzie, J.; Karpoff, A.M. Bacterially induced dolomite precipitation in anoxic culture experiments. *Geology* **2000**, *28*. [[CrossRef](#)]
22. Han, Z.; Sun, B.; Zhao, H.; Yan, H.; Han, M.; Zhao, Y.; Meng, R.; Zhuang, D.; Li, D.; Ma, Y.; et al. Isolation of *Leclercia adcarboxylata* Strain JLS1 from dolostone sample and characterization of its induced struvite minerals. *Geomicrobiol. J.* **2017**, *34*, 500–510. [[CrossRef](#)]
23. Krause, S.; Liebetrau, V.; Löscher, C.; Böhm, F.; Gorb, S.; Eisenhauer, A.; Treude, T. Marine ammonification and carbonic anhydrase activity induce rapid calcium carbonate precipitation. *Geochim. Cosmochim. Acta* **2018**, *243*. [[CrossRef](#)]
24. Ferris, F.; Fyfe, W.S.; Beveridge, T.J. Bacteria as nucleation sites for authigenic minerals in a Metal-Contaminated Lake Sediment. *Chem. Geol.* **1987**, *63*, 225–232. [[CrossRef](#)]
25. Kawaguchi, T.; Decho, A. A laboratory investigation of cyanobacterial extracellular polymeric secretion (EPS) in influencing CaCO₃ polymorphism. *J. Cryst. Growth* **2002**, *240*, 230–235. [[CrossRef](#)]
26. Yan, H.; Han, Z.; Zhao, H.; Pan, J.; Zhao, Y.; Tucker, M.; Zhou, J.; Yan, X.; Yang, H.; Fan, D. The bio-precipitation of calcium and magnesium ions by free and immobilized *Lysinibacillus fusiformis* DB1-3 in the wastewater. *J. Clean. Prod.* **2020**, *252*, 119826. [[CrossRef](#)]
27. Braissant, O.; Cailleau, G.; Dupraz, C.; Verrecchia, A. Bacterially induced mineralization of calcium carbonate in terrestrial environments: The role of exopolysaccharides and amino acids. *J. Sediment. Res.* **2003**, *73*, 485–490. [[CrossRef](#)]
28. Sanchez-Roman, M.; Rivadeneyra, M.A.; Vasconcelos, C.; McKenzie, J.A. Biomineralization of carbonate and phosphate by moderately halophilic bacteria. *FEMS Microbiol. Ecol.* **2007**, *61*, 273–284. [[CrossRef](#)]

29. Han, Z.; Yu, W.; Zhao, H.; Zhao, Y.; Tucker, M.; Yan, H. The significant roles of Mg/Ca ratio, Cl^- and SO_4^{2-} in carbonate mineral precipitation by the halophile *Staphylococcus epidermis* Y2. *Minerals* **2018**, *8*, 594. [[CrossRef](#)]
30. Guo, W.; Ma, H.; Li, F.; Jin, Z.; Li, J.; Ma, F.; Wang, C. *Citrobacter* sp strain GW-M Mediates the Coexistence of Carbonate Minerals with Various Morphologies. *Geomicrobiol. J.* **2013**, *30*, 749–757. [[CrossRef](#)]
31. Lin, C.Y.; Turchyn, A.; Steiner, Z.; Bots, P.; Lampronti, G.; Tosca, N. The role of microbial sulfate reduction in calcium carbonate polymorph selection. *Geochim. Cosmochim. Acta* **2018**, *237*. [[CrossRef](#)]
32. Han, Z.; Li, D.; Zhao, H.; Yan, H.; Li, P. Precipitation of carbonate minerals induced by the Halophilic *Chromohalobacter Israelensis* under high salt concentrations: Implications for natural environments. *Minerals* **2017**, *7*, 95. [[CrossRef](#)]
33. Han, Z.; Wang, J.; Zhao, H.; Tucker, M.E.; Zhao, Y.; Wu, G.; Zhou, J.; Yin, J.; Zhang, H.; Zhang, X.; et al. Mechanism of Biomineralization Induced by *Bacillus subtilis* J2 and Characteristics of the Biominerals. *Minerals* **2019**, *9*, 218. [[CrossRef](#)]
34. Khan, M.S.; Garnier, G. Direct measurement of alkaline phosphatase kinetics on bioactive paper. *Chem. Eng. Sci.* **2013**, *87*, 91–99. [[CrossRef](#)]
35. Garcia-Belinchón, C. Struvite recovery: Pilot-scale results and economic assessment of different scenarios. *Water Pract. Technol.* **2013**, *8*, 119–130. [[CrossRef](#)]
36. Sun, H.; Yuan, D.; Hou, X.; Wang, X.; Liu, L.; Zhang, D.; Han, Y. A novel metal-organic coordination complex crystal: Tris allylthiourea zinc bromide (ATZB) as a nonlinear optical material. *Cryst. Res. Technol.* **2007**, *42*, 65–68. [[CrossRef](#)]
37. Yang, R.; Fan, A.; Loon, T.; Han, Z.; Wang, X. Depositional and diagenetic controls on sandstone reservoirs with low porosity and low permeability in the eastern sulige gas field, China. *Acta Geol. Sin. Engl.* **2014**, *88*, 1513–1534. [[CrossRef](#)]
38. Chen, Y.; Xu, X.J.; Cui, H.Z.; Dai, K.H.; Song, Z.S.; Jiang, W.J.; Qi, L. Preferred orientation of crystals and the intensity ratios of XRD peaks of cathode material LiCoO_2 . *Acta Phys. Chim. Sin.* **2007**, *23*, 1948–1953. [[CrossRef](#)]
39. Chen, Y.; Han, Q.; Wang, Y.; Zhang, Q.; Qiao, X. Synthesis of pyridinium polysiloxane for antibacterial coating in supercritical carbon dioxide. *J. Appl. Polym. Sci.* **2014**, *132*. [[CrossRef](#)]
40. Li, T.; Yuan, C.; Zhao, Y.; Chen, Q.; Wei, M.; Wang, Y. Synthesis, characterization, and properties of aniline-p-phenylenediamine copolymers. *High Perform. Polym.* **2013**, *25*, 348–353. [[CrossRef](#)]
41. Zhang, X.Y.; Ge, S.-S.; Shao, Q.; Liu, M.; Liu, Q.Y. Synthesis and photocatalytic activity of CeO_2 hollow microspheres via yeast template route. *Chin. J. Inorg. Chem.* **2016**, *32*, 1535–1542. [[CrossRef](#)]
42. Xiangxin, K.; Jiang, Z.; Han, C.; Lijing, Z.; Zhang, Y.; Zhang, R.; Tian, J. Genesis and Implications of the Composition and Sedimentary Structure of Fine-Grained Carbonate Rocks in the Shulu Sag. *J. Earth Sci.* **2017**, *28*, 1047–1063. [[CrossRef](#)]
43. Xu, Y.; Lu, M. Microbially enhanced oil recovery at simulated reservoir conditions by use of engineered bacteria. *J. Pet. Sci. Eng.* **2011**, *78*, 233–238. [[CrossRef](#)]
44. Zhu, L.; Zhang, L.; Tang, Y.; Ma, D.; Yang, J. Synthesis of kaolin/sodium alginate-grafted poly(acrylic acid-co-2-acrylamido-2-methyl-1-propane sulfonic acid) hydrogel composite and its sorption of lead, cadmium, and zinc ions. *J. Elastom. Plast.* **2014**, *47*, 488–501. [[CrossRef](#)]
45. Jun, L.; Yao, Y.; Liu, D.; Elsworth, D. Experimental evaluation of CO_2 enhanced recovery of adsorbed-gas from shale. *Int. J. Coal Geol.* **2017**, *179*, 211–218. [[CrossRef](#)]
46. Wang, C.; Wu, Y.; Li, Y.; Shao, Q.; Yan, X.; Han, C.; Wang, Z.; Liu, Z.; Guo, Z. Flame-retardant rigid polyurethane foam with a phosphorus-nitrogen single intumescent flame retardant. *Polym. Adv. Technol.* **2017**, *29*, 668–676. [[CrossRef](#)]
47. Cui, X.; Zhu, G.; Pan, Y.; Shao, Q.; Zhao, C.; Dong, M.; Zhang, Y.; Guo, Z. Polydimethylsiloxane-titania nanocomposite coating: Fabrication and corrosion resistance. *Polymer* **2018**, *138*, 203–210. [[CrossRef](#)]
48. Yang, W.; Wang, X.-L.; Li, J.; Yan, X.; Ge, S.; Tadakamalla, S.; Guo, Z. Polyoxymethylene/ethylene butylacrylate copolymer/ethylene-methyl acrylate-glycidyl methacrylate ternary blends. *Polym. Eng. Sci.* **2018**, *58*, 1127–1134. [[CrossRef](#)]
49. Liu, F.; Csetenyi, L.; Gadd, G. Amino acid secretion influences the size and composition of copper carbonate nanoparticles synthesized by ureolytic fungi. *Appl. Microbiol. Biotechnol.* **2019**, *103*, 7217–7230. [[CrossRef](#)]
50. Chang, X.; Wang, T.G.; Li, Q.; Cheng, B.; Tao, X. Geochemistry and possible origin of petroleum in Palaeozoic reservoirs from Halahatang Depression. *J. Asian Earth Sci.* **2013**, *74*, 129–141. [[CrossRef](#)]

51. Chen, J.; Chough, S.K.; Han, Z.; Lee, J.-H. An extensive erosion surface of a strongly deformed limestone bed in the Gushan and Chaomidian formations (late Middle Cambrian to Furongian), Shandong Province, China: Sequence-stratigraphic implications. *Sediment. Geol.* **2011**, *233*, 129–149. [[CrossRef](#)]
52. Gao, L.; Han, Z.; Han, Y.; Han, C.; Wei, F.; Qin, Z. Controlling of cements and physical property of sandstone by fault as observed in well Xia503 of Huimin sag, Linnan sub-depression. *Sci. China Earth Sci.* **2013**, *56*, 1942–1952. [[CrossRef](#)]
53. Li, F.; Li, W. Petrological record of CO₂ influx in the Dongying Sag, Bohai Bay Basin, NE China. *Appl. Geochem.* **2017**, *84*, 373–386. [[CrossRef](#)]
54. Li, Y.; Chang, X.; Yin, W.; Sun, T.; Song, T. Quantitative impact of diagenesis on reservoir quality of the Triassic Chang 6 tight oil sandstones, Zhenjing area, Ordos Basin, China. *Mar. Pet. Geol.* **2017**, *86*, 1014–1028. [[CrossRef](#)]
55. Wang, G.; Chang, X.; Yin, W.; Li, Y.; Song, T. Impact of diagenesis on reservoir quality and heterogeneity of the Upper Triassic Chang 8 tight oil sandstones in the Zhenjing area, Ordos Basin, China. *Mar. Petro. Geol.* **2017**, *83*, 84–96. [[CrossRef](#)]
56. Ammann, M.; Siegwolf, R.; Pichlmayer, F.; Suter, M.; Saurer, M.; Brunold, C. Estimating the uptake of traffic-derived NO₂ from ¹⁵N abundance in Norway spruce needles. *Oecologia* **1999**, *118*, 124–131. [[CrossRef](#)]
57. Brenner, D.J.; Grimont, P.A.; Steigerwalt, A.G.; Fanning, G.R.; Ageron, E.; Riddle, C.F. Classification of *Citrobacter* by DNA hybridization: Designation of *Citrobacter farmeri* sp. nov., *Citrobacter youngae* sp. nov., *Citrobacter braakii* sp. nov., *Citrobacter werkmanii* sp. nov., *Citrobacter sedlakii* sp. nov., and three unnamed *Citrobacter* genomospecies. *Int. J. Syst. Bacteriol.* **1993**, *43*, 645–658. [[CrossRef](#)]
58. Han, Z.; Gao, X.; Zhao, H.; Tucker, M.; Zhao, Y.; Bi, Z.; Pan, J.; Wu, G.; Yan, H. Extracellular and intracellular biomineralization induced by *Bacillus licheniformis* DB1-9 at different Mg/Ca molar ratios. *Minerals* **2018**, *8*, 585. [[CrossRef](#)]
59. Ferraris, G.; Fuess, H.; Joswig, W. Neutron diffraction study of MgNH₄PO₄ · 6H₂O (struvite) and survey of water molecules donating short hydrogen bonds. *Acta Crystallogr. Sect. B* **1986**, *42*, 253–258. [[CrossRef](#)]
60. Sleator, R.D.; Gahan, C.G.; Hill, C. Identification and disruption of the proBA locus in *Listeria monocytogenes*: Role of proline biosynthesis in salt tolerance and murine infection. *Appl. Environ. Microb.* **2001**, *67*, 2571–2577. [[CrossRef](#)]
61. Nyssola, A.; Kerovuo, J.; Kaukinen, P.; Weymarn, N.; Reinikainen, T. Extreme Halophiles Synthesize Betaine from Glycine by Methylation. *J. Biol. Chem.* **2000**, *275*, 22196–22201. [[CrossRef](#)] [[PubMed](#)]
62. Liu, Y.; Yuan, Y.; Wang, W.; Wachemo, A.C.; Zou, D. Effects of adding osmoprotectant on anaerobic digestion of kitchen waste with high level of salinity. *J. Biosci. Bioeng.* **2019**, *128*, 723–732. [[CrossRef](#)] [[PubMed](#)]
63. Margesin, R.; Schinner, F. Potential of halotolerant and halophilic microorganisms for biotechnology. *Extremophiles* **2001**, *5*, 73–83. [[CrossRef](#)] [[PubMed](#)]
64. Castro, R.; Marcos, P.; Lorriaux, A.; Steil, M.; Gengembre, L.O.; Roussel, P.; Gouvea, D. Interface excess and polymorphic stability of nanosized zirconia-magnesia. *Chem. Mater.* **2008**, *20*, 3505–3511. [[CrossRef](#)]
65. Tan, Y.; Shao, Z.-B.; Chen, X.-F.; Long, J.-W.; Chen, L.; Wang, Y.-Z. A novel multifunctional organic-inorganic hybrid curing agent with high flame-retardant efficiency for epoxy resin. *ACS Appl. Mater. Interfaces* **2015**, *7*, 17919–17928. [[CrossRef](#)]
66. Bai, J.; Nagashima, T.; Yajima, T. XPS Study of Apatite Formed from Simulated Body Fluid on a Titanium Substrate Surface Nitrided by an Atmospheric Pressure Nitrogen Microwave Plasma. *J. Photopolym. Sci. Technol.* **2015**, *28*, 455–459. [[CrossRef](#)]
67. Amalric, J.; Mutin, P.; Guerrero, G.; Ponche, A.; Sotto, A.; Lavigne, J.-P. Phosphonate monolayers functionalized by silver thiolate species as antibacterial nanocoating on titanium and stainless steel. *J. Mater. Chem.* **2009**, *19*, 141–149. [[CrossRef](#)]
68. Dufrene, Y.F.; van der Wal, A.; Norde, W.; Rouxhet, P.G. X-ray photoelectron spectroscopy analysis of whole cells and isolated cell walls of gram-positive bacteria: Comparison with biochemical analysis. *J. Bacteriol.* **1997**, *179*, 1023–1028. [[CrossRef](#)]
69. Marriott, A.; Hunt, A.; Bergström, E.; Wilson, K.; Budarin, V.; Thomas-Oates, J.; Clark, J.; Brydson, R. Investigating the structure of biomass-derived non-graphitizing mesoporous carbons by electron energy loss spectroscopy in the transmission electron microscope and X-ray photoelectron spectroscopy. *Carbon* **2013**, *67*, 514. [[CrossRef](#)]

70. Ke, C.; Shi, B.; Yue, Y.; Qi, J.; Guo, L. Binary synergy strengthening and toughening of bio-inspired nacre-like graphene oxide/sodium alginate composite paper. *ACS Nano* **2015**, *9*, 8165–8175. [[CrossRef](#)]
71. Sanchez-Roman, M.; Romanek, C.S.; Fernandez-Remolar, D.C.; Sanchez-Navas, A.; McKenzie, J.A.; Amils Pibernat, R.; Vasconcelos, C. Aerobic biomineralization of Mg-rich carbonates: Implications for natural environments. *Chem. Geol.* **2011**, *281*, 143–150. [[CrossRef](#)]
72. Stephenson, A.E.; DeYoreo, J.J.; Wu, L.; Wu, K.J.; Hoyer, J.; Dove, P.M. Peptides enhance magnesium signature in calcite: Insights into origins of vital effects. *Science* **2008**, *322*, 724–727. [[CrossRef](#)] [[PubMed](#)]
73. Gaetani, G.A.; Cohen, A.L.; Wang, Z.; Crusius, J. Rayleigh-based, multi-element coral thermometry: A biomineralization approach to developing climate proxies. *Geochim. Cosmochim. Acta* **2011**, *75*, 1920–1932. [[CrossRef](#)]
74. Ma, Y.; Aichmayer, B.; Paris, O.; Fratzl, P.; Meibom, A.; Metzler, R.A.; Politi, Y.; Addadi, L.; Gilbert, P.U.P.A.; Weiner, S. The grinding tip of the sea urchin tooth exhibits exquisite control over calcite crystal orientation and Mg distribution. *Proc. Natl. Acad. Sci. USA* **2009**, *106*, 6048–6053. [[CrossRef](#)]
75. Robach, J.S.; Stock, S.R.; Veis, A. Mapping of magnesium and of different protein fragments in sea urchin teeth via secondary ion mass spectroscopy. *J. Struct. Biol.* **2006**, *155*, 87–95. [[CrossRef](#)]
76. Kluge, S.; Weston, J. Can a hydroxide ligand trigger a change in the coordination number of magnesium ions in biological systems? *Biochemistry* **2005**, *44*, 4877–4885. [[CrossRef](#)]
77. Fukushi, K.; Munemoto, T.; Sakai, M.; Yagi, S. Monohydrocalcite: A promising remediation material for hazardous anions. *Sci. Technol. Adv. Mat.* **2011**, *12*, 064702. [[CrossRef](#)]
78. Rodriguez-Blanco, J.; Shaw, S.; Bots, P.; Roncal-Herrero, T.; Benning, L. The role of Mg in the crystallization of monohydrocalcite. *Geochim. Cosmochim. Acta* **2014**, *127*, 204–220. [[CrossRef](#)]
79. Dejehet, F.; Idrissi, S.; Debuys, R. Magnesium and occluded water in calcium carbonate monohydrate. *J. Chim. Phys.* **1999**, *96*, 741–753. [[CrossRef](#)]
80. Last, F.; Last, W.; Halden, N. Carbonate microbialites and hardgrounds from Manito Lake, an alkaline, hypersaline lake in the northern Great Plains of Canada. *Sediment. Geol.* **2010**, *225*, 34–49. [[CrossRef](#)]
81. Rodriguez-Blanco, J.; Bots, P.; Roncal-Herrero, T.; Shaw, S.; Benning, L. The role of pH and Mg on the stability and crystallization of amorphous calcium carbonate. *J. Alloy. Compd.* **2012**, *536*, S477–S479. [[CrossRef](#)]
82. Delgado, G.; Párraga, J.; Martín-García, J.M.; de las Angustias Rivadeneyra, M.; Sánchez-Marañón, M.; Delgado, R. Carbonate and phosphate precipitation by saline soil bacteria in a monitored culture medium. *Geomicrobiol. J.* **2013**, *30*, 199–208. [[CrossRef](#)]
83. Rivadeneyra, M.; Martín-Algarra, A.; Sánchez-Navas, A.; Martín-Ramos, D. Carbonate and phosphate precipitation by *Chromohalobacter marismortui*. *Geomicrobiol. J.* **2006**, *23*, 1–13. [[CrossRef](#)]
84. Beavon, J.; Heatley, N. The occurrence of struvite (magnesium ammonium phosphate hexahydrate) in microbial cultures. *J. Gen. Microbiol.* **1963**, *31*, 167–169. [[CrossRef](#)]
85. Downey, J.A.; Nickel, J.C.; Clapham, L.; McLean, R.J. In vitro inhibition of struvite crystal growth by acetohydroxamic acid. *Br. J. Urol.* **1992**, *70*, 355–359. [[CrossRef](#)]
86. Wierzbicki, A.; Sallis, J.D.; Stevens, E.D.; Smith, M.; Sikes, C.S. Crystal growth and molecular modeling studies of inhibition of struvite by phosphocitrate. *Calcif. Tissue Int.* **1997**, *61*, 216–222. [[CrossRef](#)]
87. Li, H.; Yao, Q.-Z.; Wang, Y.-Y.; Li, Y.-L.; Zhou, G.-T. Biomimetic synthesis of struvite with biogenic morphology and implication for pathological biomineralization. *Sci. Rep.* **2015**, *5*, 7718. [[CrossRef](#)]
88. Basakcildan-Kabakci, S.; Thompson, A.; Cartmell, E.; Le Corre, K. Adsorption and precipitation of tetracycline with struvite. *Water Environ. Res.* **2007**, *79*, 2551–2556. [[CrossRef](#)]

